

# Comparing 1-year GUMICS–4 simulations of the Terrestrial Magnetosphere with Cluster Measurements

G. Facskó<sup>1,2,3</sup>, D. G. Sibeck<sup>2</sup>, I. Honkonen<sup>4</sup>, A. Tímár<sup>1</sup>, Y. Y. Shprits<sup>5,6</sup>,  
L. Degener<sup>4\*</sup>, P. Peitso<sup>7†</sup>, E. I. Tanskanen<sup>7</sup>, C. R. Anekallu<sup>8</sup>, J. Kalmár<sup>9</sup>,  
J. Bór<sup>9</sup>, G. Farinas Perez<sup>2,3‡</sup>, S. Szalai<sup>9,10</sup>, Á. Kis<sup>7</sup>, V. Wesztergom<sup>7</sup>,  
N. A. Aseev<sup>5,6</sup>

<sup>1</sup>Wigner Research Centre for Physics, Budapest, Hungary

<sup>2</sup>NASA Goddard Space Flight Center, Greenbelt, Maryland, USA

<sup>3</sup>the Catholic University of America, Washington DC, USA

<sup>4</sup>Finnish Meteorological Institute, Helsinki, Finland

<sup>5</sup>Helmholtz Centre Potsdam, GFZ German Research Centre for Geosciences, Potsdam, Germany

<sup>6</sup>Institute for Physics and Astronomy, University of Potsdam, Potsdam, Germany

<sup>7</sup>Aalto University, School of Electrical Engineering, Espoo, Finland

<sup>8</sup>UCL Department of Space & Climate Physics, Mullard Space Science Laboratory, Dorking, UK

<sup>9</sup>Research Centre for Astronomy and Earth Sciences, Sopron, Hungary

<sup>10</sup>University of Miskolc, Department of Geophysics, Miskolc, Hungary

## Key Points:

- The GUMICS–4 code provides realistic ion plasma moments and magnetic field in the solar wind and the outer magnetosheath.
- The code [...] predicts [...] realistic bow shock locations [...].
- An inner magnetosphere model should be added to the code to increase the accuracy of the simulation.

\*Now private individual, Hannover, Germany

†Now at Aurora Propulsion Technologies, Espoo, Finland

‡Now at University of Miami, Electrical and Computer Engineering Department, Miami, Florida, USA

Corresponding author: Gábor Facskó, gabor.i.facsko@gmail.com

23      **Abstract**

24      We compare the predictions of the GUMICS-4 global magnetohydrodynamic  
 25      model for the interaction of the solar wind with the Earth's magnetosphere  
 26      with Cluster-3 measurements over the course of one year, from January 29,  
 27      2002 to February 2, 2003. In particular, we compare the predictions with the  
 28      north/south component of the magnetic field ( $B_z$ ), the component of the ve-  
 29      locity along the Sun-Earth line ( $V_x$ ), and the plasma density as determined  
 30      from a top hat plasma spectrometer and the spacecraft's potential. We select  
 31      intervals in the solar wind, the magnetosheath and the magnetosphere where these in-  
 32      struments above provided good quality data and the **model correctly predicts the**  
 33      **region in which the spacecraft is located**. We determine the location of the bow shock,  
 34      the magnetopause and the neutral sheet **from** the spacecraft measurements and com-  
 35      pare their **locations to those predicted by the simulation**.

36      The GUMICS-4 **model** provides quite good results in the solar wind however its  
 37      accuracy is **worse** in the magnetosheath. The simulation results are not realistic in the  
 38      magnetosphere. The bow shock location is predicted well however the magnetopause lo-  
 39      cation is less accurate. The neutral sheet positions are located quite well thanks to the  
 40      special solar wind conditions. The reason for the **inaccuracy of the magnetopause**  
 41      **position and the parameters of the magnetosphere** is the missing inner magne-  
 42      tosphere model.

43      **1 Introduction**

44      One of the most cost-effective way to study the interaction of the solar wind **with**  
 45      planetary magnetospheres (or predict the conditions **in** near-Earth space) is using a global  
 46      magnetohydrodynamic (MHD) code. In the past, several [...] parallelized, effective, ver-  
 47      ified and validated codes were developed, which are used and applied to forecast the cos-  
 48      mic environment of the Earth; such as the Lyon-Fedder-Mobarry [LFM; Lyon *et al.*, 2004]  
 49      **code, the Grid Agnostic MHD for Extended Research Applications [GAM-**  
 50      **ERA; Zhang *et al.*, 2019]**, the Open Geospace General Circulation Model [OpenG-  
 51      GCM; Raeder *et al.*, 2008], the Block-Adaptive-Tree-Solarwind-Roe-Upwind-Scheme [BATS-  
 52      R-US; Powell *et al.*, 1999; Tóth *et al.*, 2012]. In Europe only three global MHD codes  
 53      were developed: the Grand Unified Magnetosphere–Ionosphere Coupling Simulation [GUMICS-4;  
 54      Janhunen *et al.*, 2012], the Computational Object Oriented Libraries for Fluid Dynam-

55 ics [COOLFluiD; *Lani et al.*, 2012] and the 3D resistive magnetohydrodynamic code Gor-  
 56 gon [*Chittenden et al.*, 2004; *Ciardi et al.*, 2007]. The COOLFluiD is a general-purpose  
 57 plasma simulation tool. The Gorgon code was developed **to study** high energy, colli-  
 58 sional plasma interactions and has been adapted to simulate planetary magnetospheres  
 59 and their interaction with the solar wind [*Mejnertsen et al.*, 2016, 2018]. **Neither GOR-**  
 60 **GON nor COOLfluid have an ionospheric solver.** The GUMICS–4 model was de-  
 61 veloped to study the solar wind-terrestrial magnetosphere interaction and its parallel ver-  
 62 sion has not been available for the scientific community **because it is still in devel-**  
 63 **opment** (see Section 2.1). **Almost all of** these codes are available at the Community  
 64 Coordinated Modelling Center (CCMC; <http://ccmc.gsfc.nasa.gov/>) hosted by the NASA  
 65 Goddard Space Flight Center (GSFC) **or** the Virtual Space Weather Modelling Centre  
 66 (VSWMC; <http://swe.ssa.esa.int/web/guest/kul-cmpa-federated>; **requires regisra-**  
 67 **tion for the European Space Agency (ESA) Space Situational Awareness (SSA)**  
 68 **Space Weather (SWE) portal**) hosted by the KU Leuven [*Poedts et al.*, 2020]. A com-  
 69 parison of the simulation results **with** spacecraft and ground-based measurements is nec-  
 70 essary to understand the abilities and features of the developed tools. **A** statistical study  
 71 using long term global MHD runs for validation [...] of the codes seems **is needed.** **Be-**  
 72 **cause** [...] providing long simulations **are** costly and time consuming [...], only a few  
 73 studies **have been** done, **all for periods much less** than a year.

74 *Guild et al.* [2008a,b] launched two months of LFM runs and compared the plasma  
 75 sheet properties in the simulated tail with the statistical properties of six years Geotail  
 76 magnetic field and plasma observations [*Kokubun et al.*, 1994; *Mukai et al.*, 1994]. The  
 77 LFM successfully reproduced the global features of the global plasma sheet in **a** statis-  
 78 tical sense. However, there were some differences. The sheet was too cold, too dense and  
 79 the bulk flow was faster than the observed plasma sheet [*Kokubun et al.*, 1994; *Mukai*  
 80 *et al.*, 1994]. The LFM overestimated the ionospheric transpolar potential. The trans-  
 81 polar potential correlated with the speed of the plasma sheet flows. The equatorial maps  
 82 of density, thermal pressure, thermal energy and velocity were compared. The LFM over-  
 83 estimated the plasma sheet density close to the Earth and underestimated the temper-  
 84 ature by a factor of ∼3. The LFM overestimated the global average flow speed by a fac-  
 85 tor of ∼2. The LFM reproduced many of the climatological features of the Geotail data  
 86 set. The low-resolution model underestimated the occurrence of the fast earthward and  
 87 tailward flows. Increasing the simulation resolution resulted in the development of fast,

88 busty flows. These flows influenced the statistics and contributed to a better  
 89 agreement between simulations and observations.

90 *Zhang et al.* [2011] [...] studied the statistics of magnetosphere-ionosphere (MI)  
 91 coupling **using *Guild et al.* [2008a]’s LFM simulation above.** The polar cap po-  
 92 tential and the field aligned currents (FAC), the downward Poynting flux and the vor-  
 93 ticity of the ionospheric convection were compared with observed statistical averages and  
 94 the Weimer05 empirical model [*Weimer*, 2005]. The comparisons showed that the LFM  
 95 model produced quite accurate average distributions of the Region 1 (R1) and Region  
 96 2 (R2) currents. The ionospheric Region 2 currents in the MHD simulation seemed to  
 97 **originate** from the diamagnetic ring current. The average LFM Region 1 and 2 currents  
 98 were **small** compared with the values from the Weimer05 model. The average CPCP  
 99 was higher in the LFM simulation than the measurements of the SuperDARN and the  
 100 Weimer05 model. The average convention pattern was quite symmetric in the LFM sim-  
 101 ulation against the SuperDARN measurements and the Weimer05 model. The Super-  
 102 DARN measurements and the Weimer05 model had **a** dawn-dusk asymmetry. In the LFM  
 103 model more Poynting flux flowed into the polar region ionosphere than in the Weimer05  
 104 model. It was the consequence of the larger CPCP in the LFM simulation. The larger  
 105 CPCP allowed **a** higher electric field in the polar region. The statistical dependence of  
 106 the high-latitude convection patterns on Interplanetary Magnetic Field (IMF) clock an-  
 107 gle was similar to the SuperDARN measurements [*Sofko et al.*, 1995] and the Weimer05  
 108 model. The average ionospheric field-aligned vorticity showed good agreement on the day-  
 109 side. However, the LFM model gave **a** larger nightside vorticity than SuperDARN mea-  
 110 surements because the Pedersen conductance on the night side ionosphere was too low.

111 *Wiltberger et al.* [2017] studied the structure of the high latitude field-aligned cur-  
 112 rent patterns using three resolutions of the LFM global MHD code and the Weimer05  
 113 empirical model [*Weimer*, 2005]. The studied period was a month long and contained  
 114 two high-speed streams. Generally, the patterns agreed well with results obtained from  
 115 the Weimer05 computing. As the resolution of the simulations increased, the currents be-  
 116 came more intense and narrow. The ratio of the Region 1 (R1), the Region 2 (R2) cur-  
 117 rents and the R1/R2 ratio increased when the simulation resolution increases. However,  
 118 both the R1 and R2 currents were smaller than the predictions of the Weimer05 model.  
 119 This effect led to a better agreement of the LFM simulation results with the Weimer 2005  
 120 model results. The CPCP pattern became concentrated in higher latitudes because of

121 the stronger R2 currents. The relationship of the CPCP and the R1 looked evident at  
 122 higher resolution of the simulation. The LFM simulation could have reproduced the sta-  
 123 tistical features of the field aligned current (FAC) patterns.

124 *Hajdusek et al. [2017]* simulated **the** month of January 2005 using the Space Weather  
 125 Modelling Framework [SWMF; *Tóth et al.*, 2005] and the OMNI solar wind data as in-  
 126 put. The simulations were done with and without **an** inner magnetosphere model and  
 127 using two different grid resolutions. The model was very good in predicting the **ring** cur-  
 128 rents [...] [SYM-H; <http://wdc.kugi.kyoto-u.ac.jp/aeasy/asy.pdf>; *Iyemori*, 1990]. The  
 129  $K_p$  index (that measures the general magnetospheric convention and the auroral currents  
 130 [*Bartels et al.*, 1939; *Rostoker*, 1972; *Thomsen*, 2004]) was predicted well during storms  
 131 however the index was over predicted during quiet time periods. The AL index (that de-  
 132 scribes the westward electro jet of the surface magnetic field introduced by *Davis and*  
 133 *Sugiura* [1966]) was predicted reasonably well **on** average, however the model reached  
 134 the highest negative AL value less often than the observations because the model cap-  
 135 tured the structure of the auroral zone currents poorly. The overpredicting of  $K_p$  index  
 136 during quiet times might have had the same reason because that index was also sensi-  
 137 tive **to** auroral zone dynamics. The SWMF usually over predicted the CPCP. These re-  
 138 sults were not sensitive to grid **resolutions**, **with the except of** the AL index, **whitch**  
 139 reached the highest negative value more often when the grid resolution was higher. Switch-  
 140 ing off of the inner magnetosphere model had **a negative effect on** the accuracy of all  
 141 quantities mentioned above, except the CPCP.

142 In this paper the Cluster SC3 measurements are compared directly to a previously  
 143 made 1-year long GUMICS–4 simulation in the solar wind, magnetosheath and the mag-  
 144 netosphere along the Cluster SC3 orbit saved from the simulation results and measured  
 145 by the spacecraft [*Facskó et al.*, 2016]. Three parameters ( $B_z$ ,  $V_X$  and  $n$ ) were studied  
 146 as well as the location of the bow shock, magnetopause and the neutral sheet. The struc-  
 147 ture of this paper is as follows. Section 2 describes the GUMICS–4 code, the 1-year sim-  
 148 ulation and the instruments. Section 3 gives comparisons between the simulations and  
 149 observations. Results of the comparison are discussed in Section 4. Finally, Section 5 con-  
 150 tains the conclusions.

151      **2 The GUMICS–4 products and Cluster measurements**

152      Here we use two [...] very different [...] time series. The first type is derived from  
 153      a previously 1-year **run of the** GUMICS–4 simulation [Facsikó *et al.*, 2016]. The sec-  
 154      ond **time series were** measured by the magnetometer, ion plasma and electric field in-  
 155      struments of the Cluster reference spacecraft.

156      **2.1 The GUMICS–4 code**

157      The GUMICS–4 has two coupled simulation domains, the magnetospheric domain  
 158      outside of  $3.7 R_E$  radius **sphere** around the Earth and a coupled ionosphere module con-  
 159      taining a 3D electron density model **for** the ionosphere. The GUMICS–4 is not a par-  
 160      allel code however it **has been** extensively used for studying the energy propagation pro-  
 161      cesses from the solar wind to the magnetosphere through the magnetopause and other  
 162      features [Janhunen *et al.*, 2012, see the references therein]. The code has also been ap-  
 163      plied **to study** forced reconnection in the tail [Vörös *et al.*, 2014]. Recently **several hun-**  
 164      **dred** synthetic two hours duration GUMICS–4 simulation **runs** were made to compare  
 165      the simulation results to empirical formulas [Gordeev *et al.*, 2013]. The agreement was  
 166      quite good however the diameter of the magnetopause [...] in the simulation **deviated**  
 167      **significantly from** observations in the tail. The [...] GUMICS–4 **simulation mag-**  
 168      **netotail** was smaller than spacecraft observed and measured. A 1-year long simulation  
 169      was made using the GUMICS–4 code [Facsikó *et al.*, 2016]. Juusola *et al.* [2014] com-  
 170      pared the ionospheric currents, fields and the cross polar cap potential (CPCP) in the  
 171      simulation **to observations from the** Super Dual Auroral Radar Network (SuperDARN)  
 172      radars [Greenwald *et al.*, 1995] and CHAMP spacecraft [Reigber *et al.*, 2002] field aligned  
 173      currents (FAC) measurements [Juusola *et al.*, 2007; Ritter *et al.*, 2004]. The agreement  
 174      was good **for** the seasonal variation of the CPCP however the FAC and other currents  
 175      could not be reproduced properly. The possible cause of this bad agreement could be the  
 176      lack of **an** inner magnetosphere model **incorporating the physics in this region**. This  
 177      statement is supported by the result of Haiducek *et al.* [2017]. Haiducek *et al.* simulated  
 178      only a month using **a** different spatial resolution and [...] **tested** the code **with** the in-  
 179      ner magnetosphere model of the SWMF **switched off** for a special run. This run with-  
 180      out **an** inner magnetosphere model made it clear that only the CPCP parameter of the  
 181      simulation agreed quite well with the measurements. This fact explained why the agree-  
 182      ment between the Cluster SC3 and the GUMICS-4 simulations was so good as described

183 by **Lakka et al.** [2018a,b] based on the CPCP in GUMICS–4 simulations. *Kallio and*  
 184 *Facskó* [2015] determined **plasma and magnetic field** parameters along the **lunar** or-  
 185 **bit from** the *Facskó et al.* [2016]’s global MHD simulations. The [...] parameters dif-  
 186 fered significantly in the geotail **indicating a need for** future studies. *Facskó et al.* [2016]  
 187 determined the footprint of [...] Cluster SC3 using the 1-year simulation and the Tsy-  
 188 ganenko T96 empirical model [*Tsyganenko*, 1995]. The code seemed to react slower to  
 189 the dynamic changes of the solar wind pressure than the empirical model. The agree-  
 190 ment of the footprint **was** better in the Northern Hemisphere. The GUMICS–4 tail **was**  
 191 shorter in the simulations than the observations. Finally, the Y component of the inter-  
 192 planetary magnetic field twisted the simulated tail hence the agreement of the empir-  
 193 ical and computational footprints was worse **when** such solar wind conditions **prevailed**.

194 **One** workpackage of the European Cluster Assimilation Technology (ECLAT) project  
 195 ([https://cordis.europa.eu/result/rcn/165813\\_en.html](https://cordis.europa.eu/result/rcn/165813_en.html); <http://www.eclat-project.eu/>) was  
 196 the creation and analysis of a 1-year global MHD simulation using the OMNI solar wind  
 197 data from January 29, 2002 to February 2, 2003 as input **to** the GUMICS–4 code [*Facskó*  
 198 *et al.*, 2016]. The GUMICS-4 was a single core system [*Janhunen et al.*, 2012] hence the  
 199 1-year simulation was made in 1860 independent runs. This interval covered 155 Clus-  
 200 ter SC3 orbits and each orbit lasted 57 hours. The supercomputer had 12 CPUs on each  
 201 node hence the 57 hours were divided into 4.7 hours simulation time with one hour ini-  
 202 tialisation period. Each **sub-interval** used its own **individual** average Geocentric So-  
 203 lar Ecliptic (GSE) IMF magnetic field X component  $B_x$  component and dipole tilt an-  
 204 gle. All data gaps of the input file were filled using interpolation. If the data gap of the  
 205 input file was at the beginning (or the end) **of the** interval **then** the first (or last) good  
 206 data **from** the input file was used to fill the gap. The initialisation of each **simulation**  
 207 **run** was made using constant values. These values were the first valid data of the in-  
 208 put file repeated 60 times (60 minutes) in the input file of the sub-interval. The simu-  
 209 lation results were saved [...] every five minutes. Various simulation parameters, for  
 210 example, the density, particle density, temperature, magnetic field, solar wind velocity  
 211 (29 different quantities) were saved from the simulation results along the Cluster refer-  
 212 ence spacecraft’s **orbit** in the GSE coordinates. In this paper these parameters, namely  
 213 the  $B_z$ , **the north/south component of the** magnetic field **in GSE coordinates**,  
 214 the solar wind velocity GSE X component ( $V_x$ ) and the solar wind density  $n$  are com-  
 215 compared to the Cluster SC3 measurements. These parameters are selected because [...]

216  $B_z$  controls the magnetosphere, [...]  $V_x$  is the main **component of the** solar wind ve-  
217 locity [...] and [...]  $n$  is the ion plasma momentum that is the easiest to calculate; fur-  
218 thermore more instruments could determine it (see Section 2.2).

219 **2.2 The Cluster SC3 measurements**

220 The Cluster-II spacecraft of the European Space Agency (ESA) were launched in  
221 2000 and study the geospace [...] [Credland *et al.*, 1997; Escoubet *et al.*, 2001]. **The**  
222 four spacecraft form a tetrahedron however here we use only the measurements of the  
223 reference spacecraft, [...] Cluster SC3. The spacecraft were stabilised [...] and **their**  
224 period is  $\sim 4$  s. Hence, the **intrinsic time** resolution of the plasma instruments **is** 4 s and  
225 we use 4 s averaged magnetic field data. The **highest** resolution of the Cluster FluxGate  
226 Magnetometer (FGM) magnetic field instrument **is** 27 Hz [Balogh *et al.*, 1997, 2001]. The  
227 ion plasma data **are** provided by the Cluster Ion Spectrometry (CIS) Hot Ion Analyser  
228 (HIA) sub-instrument [Reme *et al.*, 1997; Rème *et al.*, 2001]. The CIS HIA instrument  
229 is calibrated using the Waves of HIgh frequency Sounder for Probing the Electron den-  
230 sity by Relaxation (WHISPER) wave instrument onboard Cluster [Décréau *et al.*, 2001;  
231 Trotignon *et al.*, 2010; Blagau *et al.*, 2013, 2014]. **The results of these** calibrations **can**  
232 **appeare** as sudden non-physical jumps in the CIS HIA data. The CIS HIA had differ-  
233 ent modes to measure in the solar wind and the magnetosphere. When the instrument  
234 switched from **one** mode to another mode it appeared as a non-physical **jumps also ap-**  
235 **pear** in the **measurements** [...]. These features **impair** the accuracy of [...] data  
236 **analyses**.

237 We protect our results from these non-physical jumps [...] using a density deter-  
238 mination based on different principles. We use the spacecraft potential of the Electric  
239 Field and Wave Experiment [EFW ; Gustafsson *et al.*, 1997, 2001] to determine the elec-  
240 tron density. This quantity can be calculated using the empirical density formula

$$n_{EFW} = 200(V_{sc})^{-1.85}, \quad (1)$$

241 where  $n_{EFW}$  is the calculated density and  $V_{sc}$  is the Cluster EFW spacecraft potential  
242 [Trotignon *et al.*, 2010, 2011]. The EFW and the WHISPER were used for the calibra-  
243 tion of the CIS HIA and the Plasma Electron and Current Experiment [PEACE; John-  
244 stone *et al.*, 1997; Fazakerley *et al.*, 2010a,b]. Both instruments were still working on-

245 board all Cluster spacecraft. Their stable operation reduced the number of data gaps;  
 246 furthermore made the data analysis easier.

### 247 3 Comparison of measurements to simulation

248 The [...] parameters **saved** from the GUMICS–4 simulations and the Cluster SC3  
 249 magnetic field, solar wind velocity and density measurements are compared in **differ-**  
 250 **ent regions, namely** the solar wind, magnetosheath and magnetosphere using cross  
 251 correlation calculation. The **temporal** resolution of the simulated Cluster orbit data is  
 252 mostly five minutes because the simulations are saved [...] every five minutes [Fazekas  
 253 *et al.*, 2016]. However, the time difference between points **can** be more than five min-  
 254 utes at the boundary of the subintervals, because the length of **the** simulation intervals  
 255 is determined in minutes. To facilitate analysis of the simulation results, all simulation  
 256 data were interpolated to one minute resolution. This method does not provide extra  
 257 information to the cross correlation calculation. The data gaps are eliminated using in-  
 258 terpolation [...] and extrapolation when the gap is at the start or the end of the selected  
 259 interval. The spin resolution (4 s) of Cluster SC3 magnetic field measurements is aver-  
 260 aged over one minute around ( $\pm 30\text{ s}$ ) the time stamps of the saved data.

261 For the correlation calculation, intervals are selected carefully in the solar wind (**see**  
 262 **Section 3.1**), the magnetosheath (**see Section 3.2**), the dayside and the night side mag-  
 263 netosphere (**see Section 3.3**). In these intervals the parameters did not vary a lot and  
 264 **we require** neither [...] Cluster nor the virtual probe **to cross** any boundaries. To  
 265 compare [...] the  $B_z$  magnetic field,  $V_x$  solar wind speed and the  $n_{CIS}$  and the  $n_{EFW}$   
 266 curves we [...] cross **correlate** selected intervals. Sometimes we get very **poor cor-**  
 267 **relation**. We carefully examine **such** cases and remove [...] short intervals (shorter  
 268 than four hours) [...] and large data gaps from the correlation calculation. (The data  
 269 gaps are interpolated however they cause loss of information.) Those intervals are also  
 270 neglected where the plasma instrument has a calibration error or changes its mode from  
 271 magnetosphere to solar wind (for example). The electron density is also calculated us-  
 272 ing [...] Equation 1 and [...] correlated [...]. We want to avoid **the** calibration er-  
 273 rors and sudden non-physical jumps mentioned previously. The **correlation results for**  
 274 **the density derived from the electric field potential** results do not differ signif-  
 275 icantly **from those for the top hat plasma instrument**, however the  $n_{EFW}$  does

276 not have any mode change and it is applicable in the magnetosphere too (against the  
 277 CIS HIA instrument).

278 **3.1 Solar wind**

279 We use OMNI IMF and solar wind velocity, density and temperature data as in-  
 280 put to the simulation. **There is a reason why we compare parameters in the**  
 281 **solar wind region in the simulation and the measurements.** The IMF X component can-  
 282 not be given to the GUMICS–4 as input [Janhunen et al., 2012; Fazekas et al., 2016]. How-  
 283 ever the magnetic field of the solar wind has an X component in the simulations. Ad-  
 284 ditionally the solar wind structure might change from the simulation domain boundary  
 285 at  $+32 R_E$  to the sub-solar point of the terrestrial bow shock where all OMNI data is  
 286 shifted. Almost the same solar wind intervals are used as in [...] Table 1 of Fazekas et al.  
 287 [2016]. The number of these intervals is small because [...] Cluster fleet instruments  
 288 were calibrated in 2002, just after **launch** (Table 1). Hence we do not have a satis-  
 289 factory ion plasma data coverage for this year. Additionally, to improve the accuracy of the  
 290 correlation calculation (see below) we delete the intervals that were too short (shorter  
 291 than five hours) or the CIS HIA instrument changed its mode. The Cluster fleet is lo-  
 292 cated in the solar wind only from December to May and only for a couple of hours dur-  
 293 ing each orbit near [...] apogee. We double check whether the Cluster SC3 stays in the  
 294 solar wind in both the simulation and reality. We also check the omnidirectional CIS HIA  
 295 ion spectra on the Cluster Science Archive (CSA; <https://www.cosmos.esa.int/web/csa/csds-quicklook-plots>). Hence 17 intervals are left in the solar wind to study (Figure 1).

297 The selected intervals **occur for** quiet solar wind conditions (Figure 2). The GUMICS–4  
 298 simulation results have five minutes resolution and the Cluster SC3 measurements have  
 299 one minute resolution (Figure 3). The measurements vary significantly. In spite of the  
 300 quiet conditions the solar wind density often changes and deviates from the simulation.  
 301 [...] Figure 4c **shows that** both densities deviate significantly. The CIS HIA density  
 302 deviation is larger as [...] expected **given** the complexity and the large number of work-  
 303 ing modes of the CIS instrument. The magnetic field and the solar wind velocity fit bet-  
 304 ter. [...] Figure 5a **shows that** the correlation of the magnetic fields is very good; fur-  
 305 thermore on Figure 5c, 5e, 5f the correlation of the solar wind velocity and density is ex-  
 306 cellent (Table 1). The time shift on Figure 5b, Figure 5d, Figure 5f is about five min-

utes for the magnetic field and the CIS data. On Figure 5h for the EFW data the time shift is worse. It is not determined as well as the other parameters.

### 309      3.2 Magnetosheath

310      The Cluster SC3 spent only a little time in the solar wind from December, 2002  
 311      to May, 2003. However, the [...] spacecraft **enters** the magnetosheath each orbit (Figure 6). We selected intervals when the value of the magnetic field is around 25 nT. The  
 312      field should be fluctuating because of the turbulent **deflected** flow of the **shocked** so-  
 313      lar wind [...] the **temperature should be greater than that in the solar wind** [...].  
 314      The **velocity should decrease to values ranging from** 100-300 km/s. The density  
 315      of the plasma **should increase** and reached **values of** 10-20 cm<sup>-3</sup>. The narrow band  
 316      on the omnidirectional CIS HIA ion spectra from the CSA (<https://www.cosmos.esa.int/web/csa/csds-quicklook-plots>) **widens from the solar wind to the magnetosheath**. 15–30 minutes  
 317      **from each bow shock** crossing we considered the Cluster SC3 to **have entered** into  
 318      the magnetosheath. At the inner **magnetopause** boundary **of the magnetopause** the  
 319      flow speed [...] and the density **drop**. The magnetic field **strength increases** and the  
 320      **magnetic field becomes** less turbulent than in the magnetosheath. The wide band on  
 321      the the omnidirectional CIS HIA ion spectra disappears. 15-30 minutes before the ap-  
 322      pearance of these indicators of the magnetopause crossing our intervals end. All inter-  
 323      vals contain large data gaps, non-physical jump **in** instrument modes [...] or **lasting**  
 324      **less** than four hour are removed. Hence 74 intervals considered in our final selection (Ta-  
 325      ble 2).

326      All intervals have quiet upstream (or input) solar wind conditions (Figure 7). **Inspection**  
 327      **of our selected** [...] magnetic field and [...] plasma parameters and the calculated em-  
 328      pirical density **indicate that they** vary significantly stronger than in the solar wind in-  
 329      tervals (Figure 8). The deviation **between** the simulated and the observed data is **also**  
 330      larger in this region [...] . The **scatter** plots of the magnetic field, plasma flow speed  
 331      and the densities **show that these parameters agree well, but with greater vari-**  
 332      **ation** than the **scatter** plots **for** the solar wind (Figure 9a, 9b, 9c). The correlation of  
 333      the simulated and the observed data is good for the magnetic field (Figure 10a), very  
 334      good for the ion plasma moments and the calculated density (Figure 10c, 10e, 10g). The  
 335      timeshift of the magnetic field is within five minutes mostly (Figure 10b) however the  
 336      timeshift of the ion plasma moments is scattered (Figure 10d, 10f). The timeshift of the  
 337      timeshift of the ion plasma moments is scattered (Figure 10d, 10f). The timeshift of the  
 338      timeshift of the ion plasma moments is scattered (Figure 10d, 10f). The timeshift of the

339 calculated EFW density seems to be more accurate (Figure 10h). Generally, the GUMICS–4  
 340 is less accurate in the magnetosheath **than in the solar wind. The modelled mag-**  
 341 **netic field is closer to the observations than the modelled plasma parameters**  
 342 **are.** The calculated empirical EFW density ( $n_{EFW}$ ) fits better than the CIS HIA den-  
 343 sity ( $n_{CIS}$ ).

344 **3.3 Magnetosphere**

345 To select intervals in the magnetosphere we looked for the CIS HIA **omnidirectional**  
 346 **ion flux spectrum.** Where the band of the hot magnetosheath ion population (dis)appeared,  
 347 the magnetosphere started/finished. The **plasma** density **decreases toward** zero, the  
 348 magnetic field **strength is large.** We left 15–30 min after/before the magnetopause trans-  
 349 sition to **identify** magnetosphere **intervals.** This way we found 132 intervals in the mag-  
 350 netosphere (Table 3) using Cluster SC3 measurements. [...] Cluster SC3 spends con-  
 351 siderable time in the magnetosphere (Figure 11).

352 Here we show neither any correlation calculation nor comparison plot. In the mag-  
 353 netosphere the GUMICS–4 does not work well. Neither the magnetic field nor the plasma  
 354 moments nor the  $N_{EFW}$  fit well. The solar wind velocity does not reach zero in the sim-  
 355 ulation. Instead the solar wind enters to the night side magnetosphere. The solar wind  
 356 CIS HIA ion plasma density and the calculated density from spacecraft potential increase  
 357 closer to the Earth (plasmasphere). The GUMICS–4 density is low there. We calculated  
 358 the dipole field in GSE using Tsyganenko geotool box [Tsyganenko, 1995] and substracted  
 359 from both the observed and the simulated magnetic field  $B_z$  data. The correlation of these  
 360 corrected magnetic field measurements and simulations is very low too.

361 **3.4 Bow shock, magnetopause, neutral sheet**

362 **77** intervals are selected when [...] Cluster SC3 crossed the terrestrial bow shock  
 363 once or multiple times (**Table 6**). When the spacecraft crosses the bow shock **inbound**  
 364 the magnitude of the magnetic field and the solar wind density increases **by a factor**  
 365 **of** 4–5 times (from 5 nT or  $5 \text{ cm}^{-3}$ , respectively), the solar wind speed drops from 400–  
 366 600 km/s to 100–300 km/s; furthermore the narrow band on the omnidirectional Clus-  
 367 ter CIS HIA ion spectra [...] widens. The Cluster measurements are 1-min averaged  
 368 **whereas** the GUMICS–4 simulations have 5-min resolution. Hence all bow shock tran-

369 sitions of the virtual spacecraft are slower and smoother. Additionally, the multiple bow  
 370 shock transitions are not visible in the GUMICS simulations. The code reacts slowly for  
 371 such sudden changes. The magnetic signatures fit better than the calculated plasma mo-  
 372 ments. The jump of the ion plasma parameters and the derived Cluster EFW density  
 373 of the simulations are shifted to the measurements. Generally, the density and the ve-  
 374 locity of the simulations seem to be less accurate than the magnetic field of the simu-  
 375 lations.

376       **54** intervals are selected around magnetopause crossings [...] (**Table 7**). When  
 377 the spacecraft crosses the magnetopause **inbound** the magnitude of the magnetic field  
 378 increases, the solar wind speed drops from 100–300 km/s to zero, the plasma density be-  
 379 comes zero; furthermore the wide band on the omnidirectional Cluster CIS HIA ion spec-  
 380 tra disappears. [...] The location of the magnetopause is well determined by the Clus-  
 381 ter SC3 measurements. However, it is very difficult to identify the magnetopause cross-  
 382 ings in the simulation data. [...] The magnetopause crossings very often cannot be seen  
 383 in the simulations. Or when the magnetopause crossings are clearly identified in both  
 384 simulations and spacecraft measurements the events are shifted. The accuracy of the model  
 385 is lower for the dayside magnetopause locations.

386       Nine intervals are chosen around Cluster SC3 neutral sheet crossings (Figure 12;  
 387 Table 8). The neutral **sheet** locations **are** determined using the results of the Bound-  
 388 ary Layer Identification Code (BLIC) Project [*Facskó et al.*, in preparation]. The BLIC  
 389 code determines the neutral sheet crossing Cluster FGM magnetic field measurements  
 390 using *Wang and Xu* [1994]’s method. When the solar wind speed is almost zero; further-  
 391 more the CIS HIA density and the EFW calculated density are almost zero too; finally  
 392 the GSE Z component of the magnetic field changes is a sign of the code indicated neu-  
 393 tral sheet crossing (Figure 20; red and blue curves). Surprisingly the neutral sheet cross-  
 394 ings are visible very well in the GUMICS simulations (Figure 20; black curves). For five  
 395 events (from nine Cluster SC3 crossings) the GUMICS–4 also provides similar smoothed  
 396 parameters and change of sign of the  $B_z$  component. This is a **outstanding** result be-  
 397 cause the tail in the GUMICS–4 simulations is significantly smaller than the observed  
 398 reality [*Gordeev et al.*, 2013; *Facskó et al.*, 2016]; furthermore the solar wind enters the  
 399 tail in MHD simulations generally [*Kallio and Facskó*, 2015].

400      **4 Discussion**

401      The agreement of [...]  $B_z$ ,  $V_x$  and  $n_{EFW}$  **in the solar wind** with the similar GU-  
 402      MICS simulation **predictions** is very good (Figure 4a, 4b, 4c, blue). The agreement of  
 403      [...]  $n_{CIS}$  is worse (Figure 4c, red). It was expected because the  $n_{EFW}$  depends on the  
 404      spacecraft potential provided by the EFW instrument. However, the CIS instrument has  
 405      many modes for measuring the plasma parameters and it needs **periodic** calibration too.  
 406      The correlation of the solar wind  $V_x$ ,  $n_{CIS}$  and  $n_{EFW}$  with the similar GUMICS sim-  
 407      ulation parameters is greater than 0.9 (Figure 5c, 5e, 5g). The correlation of the  $B_z$  is  
 408      also greater than 0.8 (Figure 5a). [...] The **upstream boundary** of the GUMICS-4  
 409      code **lies** at  $32 R_E$  [Janhunen et al., 2012], the nose of the terrestrial bow shock is at about  
 410       $20 R_E$ . If the solar wind speed is 400 km/s, then this spatial distance means less than  
 411      a 5 minutes delay, so it should not be visible. 80% of the intervals support this theory  
 412      but 20% **do** not. In these cases the one-minute resolution  $B_z$ ,  $n_{CIS}$  or the  $n_{EFW}$  pa-  
 413      rameters have a sudden jump or variation that the simulation cannot follow, or the res-  
 414      olution of the simulation data (5 minutes) is too small to see these variations. Therefore,  
 415      the correlation calculation is not accurate in these cases. Previously the OMNI data was  
 416      compared to the Cluster data and the Cluster measurements were compared to the GUMICS-4  
 417      [Fazekas et al., 2016]. The comparison suggests that the GUMICS-4 results should be  
 418      similar **for** the OMNI data. Furthermore, we calculate correlation functions in the so-  
 419      lar wind, where there is no significant perturbation of the input parameters in the sim-  
 420      ulation box. Therefore, we get **the** expected result after comparing the two different cor-  
 421      relation calculations.

422      In the magnetosheath we get worse agreement with the GUMICS simulation data  
 423      (Figure 9a, 9b, 9c). **While the parameters are correlated, the scatter is greater.**  
 424      The general reason **for** this larger uncertainty seems to be [...] **that the magnetosheath**  
 425      **is turbulent**. This phenomena explains the higher variations of the  $B_z$  magnetic field  
 426      on Figure 9a. The solar wind  $V_x$ ,  $n_{CIS}$  and  $n_{EFW}$  agree better than the magnetic field  
 427      component (Figure 9b, 9c). Here there is no deviation between the densities derived in  
 428      different ways ( $n_{CIS}$  and  $n_{EFW}$ ) on Figure 9c. Figure 10 seems to contradict these state-  
 429      ments above. The larger uncertainty of the  $B_z$  is visible on Figure 10a. However, that  
 430      correlation is still good on Figure 10b. The other parameters have larger ( $> 0.9$ ) cor-  
 431      relation in Figure 10c, 10e, 10g. However, the time shifts in Figure 10d, 10f, 10h seem  
 432      to be worse. Actually here the time shifts are worse because the shape of the time se-

433      ries in the magnetosheath looks very **smooth and similar** hence there is not enough  
 434      **points to get a sharp and large maximum correlation as the function of timeshift.**  
 435      The difference between the minimum and the maximum of the correlation  
 436      is small comparing with the uncertainty of the calculation. The maximum,  
 437      the timeshift could be anywhere and the shape of the correlation vs. timeshift  
 438      function is often neither symmetric nor has only one local maximum. Hence,  
 439      the correlation calculation provides larger time shifts for the ion plasma parameters and  
 440      the  $n_{EFW}$ .

441      In the magnetosphere the GUMICS–4 does not work well. [...] GUMICS–4 uses  
 442      a tilted dipole to describe the terrestrial magnetic field [Janhunen *et al.*, 2012]. After re-  
 443      moving the magnetic dipole from the magnetic field measurements of the Cluster SC3  
 444      and the simulation we get very low correlations and unacceptable time shifts (not shown).  
 445      [...] The tilted dipole is an insufficient description **of the inner magnetospheric mag-**  
 446      **netic field.** However, the plasma **moments** and the  $n_{EFW}$  do not fit either. The MHD  
 447      approach lost its validity in the inner magnetosphere domain therefore [...]  $V_x$  and [...]  
 448       $n$  **in** the simulations do not agree **with**  $V_x$ , [...]  $n_{CIS}$  and the  $n_{EFW}$  measured by the  
 449      Cluster SC3. Within the  $3.7 R_E$  domain **ring current physics must be added, as**  
 450      **it has been** in other global MHD codes [Lyon *et al.*, 2004; Raeder *et al.*, 2008; Powell  
 451      *et al.*, 1999; Tóth *et al.*, 2012]. This result explains the limited accuracy of the cross po-  
 452      lar cap potential (CPCP) and geomagnetic indices of the GUMICS simulations [Juusola  
 453      *et al.*, 2014]. The CPCP [...] GUMICS **agrees well with** spacecraft measurements there-  
 454      fore this quantity could be used for [...] simulation studies [Lakka *et al.*, 2018a]. Haiducek  
 455      *et al.* [2017] also [...] **compared** [...] geomagnetic indices and the CPCP. The Space  
 456      Weather Modelling Framework (SWMF) was tested. When the inner magnetosphere model  
 457      was switched off in the simulation only the comparison of the simulated and observed  
 458      CPCP was good. Therefore, the reason of the discrepancy of the geomagnetic indices  
 459      in the GUMICS simulations must be the missing inner magnetosphere model.

460      **The reason of why simulation results and [...] measurements disagree**  
 461      **could be the code or the bad input parameters. During the 1-year run the**  
 462      **distributions of the OMNI solar wind magnetic field  $B_x$ ,  $B_y$ ,  $B_z$  components**  
 463      **(Figure 13a, 13b, 13c); solar wind velocity  $V_x$ ,  $V_y$   $V_z$  components (Figure 13d, 13e, 13f)**  
 464      **and the solar wind  $P$  dynamic pressure are calculated (Figure 13g) from Jan-**  
 465      **uary 29, 2002 to February 2, 2003 in GSE reference frame. The intervals when**

466 the GUMICS–4 simulations and the Cluster SC3 measurements disagreed  
 467 are collected for intervals in the solar wind (Table 4) and the magnetosheath  
 468 (Table 5). The averaged shifted OMNI parameters of the poorly agreeing in-  
 469 tervals from the Tables 4 and 5 are saved. The distributions of the OMNI  
 470 parameters belonging to the bad simulation results are calculated for the so-  
 471 lar wind region (Figure 14, 15 and 16) and in the magnetosheath (Figure 17, 18 and 19).

472 1. In the solar wind the distributions of the OMNI  $B_x$ ,  $B_y$  and  $B_z$  can be  
 473 compared in Figure 13a and Figure 14a, 14d, 14g, 14j; Figure 13b and  
 474 Figure 14b, 14e, 14h, 14k; furthermore in Figure 13c and Figure 14c, 14f, 14i, 14l.

- 475 (a) When the  $B_z$  disagrees in simulations and measurements in Figure 14a, 14b, 14c  
 476 the distributions of the OMNI  $B_x$ ,  $B_y$  and  $B_z$  are not similar to the  
 477 distributions of the OMNI  $B_x$ ,  $B_y$  and  $B_z$  in Figure 13a, 13b and 13c.  
 478 The reason of these strange spikes is that there is only one poorly cor-  
 479 related interval for the  $B_z$  in the solar wind according to Table 4.
- 480 (b) When the  $V_x$  disagrees in simulations and measurements in Figure 14d, 14e, 14f  
 481 the distributions of the OMNI  $B_x$ ,  $B_y$  and  $B_z$  are similar to the dis-  
 482 tributions of the OMNI  $B_x$ ,  $B_y$  and  $B_z$  in Figure 13a, 13b and 13c.  
 483 The distributions do not agree perfectly because in Table 4 the num-  
 484 ber of the poorly correlated intervals is only six for the  $V_x$  component.
- 485 (c) When the  $n_{CIS}$  disagrees in simulations and measurements in Figure 14g, 14h, 14i  
 486 the distributions of the OMNI  $B_x$ ,  $B_y$  and  $B_z$  are similar to the dis-  
 487 tributions of the OMNI  $B_x$ ,  $B_y$  and  $B_z$  in Figure 13a, 13b and 13c.  
 488 The distributions do not agree perfectly because in Table 4 the num-  
 489 ber of the poorly correlated intervals is only 12 for the  $n_{CIS}$ .
- 490 (d) When the  $n_{EFW}$  disagrees in Figure 14j, 14k, 14l the distributions of  
 491 the OMNI  $B_x$ ,  $B_y$  and  $B_z$  are similar to the distributions of the OMNI  
 492  $B_x$ ,  $B_y$  and  $B_z$  in Figure 13a, 13b and 13c. The distributions do not  
 493 agree perfectly because in Table 4 the number of the poorly corre-  
 494 lated intervals is only nine for  $n_{EFW}$ .

495 The values of the OMNI  $B_x$ ,  $B_y$  and  $B_z$  are not peculiar in the solar wind.

496     **2. In the solar wind the distributions of the OMNI  $V_x$ ,  $V_y$  and  $V_z$  can be**  
 497     **compared in Figure 13d and Figure 15a, 15d, 15g, 15j; Figure 13e and**  
 498     **Figure 15b, 15e, 15h, 15k; furthermore in Figure 13f and Figure 15c, 15f, 15i, 15l.**

- 499     (a) When the  $B_z$  disagrees in Figure 15a, 15b, 15c the distributions of  
 500       the OMNI  $V_x$ ,  $V_y$  and  $V_z$  are not similar to the distributions of the OMNI  
 501        $V_x$ ,  $V_y$  and  $V_z$  in Figure 13d, 13e and 13f. The reason of these strange  
 502       spikes is that there is only one poorly correlated interval for the  $B_z$   
 503       in the solar wind according to Table 4.
- 504     (b) When the  $V_x$  disagrees in simulations and measurements in Figure 15d, 15e, 15f  
 505       the distributions of the OMNI  $V_x$ ,  $V_y$  and  $V_z$  are similar to the dis-  
 506       tributions of the OMNI  $V_x$ ,  $V_y$  and  $V_z$  in Figure 13d, 13e and 13f. The  
 507       distributions do not agree perfectly because in Table 4 the number  
 508       of the poorly correlated intervals is only six for the  $V_x$  component.
- 509     (c) When the  $n_{CIS}$  disagrees in Figure 15g, 15h, 15i the distributions of  
 510       the OMNI  $V_x$ ,  $V_y$  and  $V_z$  are similar to the distributions of the OMNI  
 511        $V_x$ ,  $V_y$  and  $V_z$  in Figure 13d, 13e and 13f. The distributions do not agree  
 512       perfectly because in Table 4 the number of the poorly correlated in-  
 513       tervals is only 12 for the  $n_{CIS}$ .
- 514     (d) When the  $n_{EFW}$  disagrees in simulations and measurements in Fig-  
 515       ure 15j, 15k, 15l the distributions of the OMNI  $V_x$ ,  $V_y$  and  $V_z$  are sim-  
 516       ilar to the distributions of the OMNI  $V_x$ ,  $V_y$  and  $V_z$  in Figure 13d, 13e  
 517       and 13f. The distributions do not agree perfectly because in Table 4  
 518       the number of the poorly correlated intervals is only nine for the  $n_{EFW}$ .

519       The values of the OMNI  $V_x$ ,  $V_y$  and  $V_z$  are not peculiar in the solar wind.

520     **3. In the solar wind the distributions of the OMNI  $P$  can be compared in**  
 521     **Figure 13g and Figure 16a, 16b, 16c, 16d.**

- 522     (a) When the  $B_z$  disagrees in Figure 16a the distribution of the OMNI  
 523        $P$  is not similar to the distribution of the OMNI  $P$  in Figure 13g. The  
 524       reason of these strange spike is that there is only one poorly corre-  
 525       lated interval for the  $B_z$  in the solar wind according to Table 4.
- 526     (b) When the  $V_x$  disagrees in simulations and measurements in Figure 16b  
 527       the distribution of the OMNI  $P$  is similar to the distributions of the

528 OMNI  $P$  in Figure 13g. The distributions do not agree perfectly be-  
 529 cause in Table 4 the number of the poorly correlated intervals is only  
 530 six  $V_x$  component.

- 531 (c) When the  $n_{CIS}$  disagrees in simulations and measurements in Figure 16c  
 532 the distribution of the OMNI  $P$  is similar to the distributions of the  
 533 OMNI  $P$  in Figure 13g. The distributions do not agree perfectly be-  
 534 cause in Table 4 the number of the poorly correlated intervals is only  
 535 12 for the  $n_{CIS}$ .
- 536 (d) When the  $n_{EFW}$  disagrees in simulations and measurements in Fig-  
 537 ure 16d the distribution of the OMNI  $P$  is similar to the distributions  
 538 of the OMNI  $P$  in Figure 13g. The distributions do not agree per-  
 539 fectly because in Table 4 the number of the poorly correlated inter-  
 540 vals is only nine for the  $n_{EFW}$ .

541 The values of the OMNI  $P$  are not peculiar in the solar wind.

542 4. In the magnetosheath the distributions of the OMNI  $B_x$ ,  $B_y$  and  $B_z$  can  
 543 be compared in Figure 13a and Figure 17a, 17d, 17g, 17j; Figure 13b  
 544 and Figure 17b, 17e, 17h, 17k; furthermore in Figure 13c and Figure 17c, 17f, 17i, 17l.

- 545 (a) When the  $B_z$  disagrees in simulations and measurements in Figure 17a, 17b, 17c  
 546 the distributions of the OMNI  $B_x$ ,  $B_y$  and  $B_z$  are similar to the dis-  
 547 tributions of the OMNI  $B_x$ ,  $B_y$  and  $B_z$  in Figure 13a, 13b and 13c.
- 548 (b) When the  $V_x$  disagrees in simulations and measurements in Figure 17d, 17e, 17f  
 549 the distributions of the OMNI  $B_x$ ,  $B_y$  and  $B_z$  are similar to the dis-  
 550 tributions of the OMNI  $B_x$ ,  $B_y$  and  $B_z$  in Figure 13a, 13b and 13c.
- 551 (c) When the  $n_{CIS}$  disagrees in simulations and measurements in Figure 17g, 17h, 17i  
 552 the distributions of the OMNI  $B_x$ ,  $B_y$  and  $B_z$  are similar to the dis-  
 553 tributions of the OMNI  $B_x$ ,  $B_y$  and  $B_z$  in Figure 13a, 13b and 13c.
- 554 (d) When the  $n_{EFW}$  disagrees in Figure 17j, 17k, 17l the distributions of  
 555 the OMNI  $B_x$ ,  $B_y$  and  $B_z$  are similar to the distributions of the OMNI  
 556  $B_x$ ,  $B_y$  and  $B_z$  in Figure 13a, 13b and 13c.

557 The distributions agree quite well because in Table 5 the number of the  
 558 poorly correlated intervals 18, 50, 33 and 30 for the  $B_z$ , the  $V_x$ , the  $n_{CIS}$   
 559 and  $n_{CIS}$  components, respectively. The number of cases are higher and

560 the values of the OMNI  $B_x$ ,  $B_y$  and  $B_z$  are not peculiar in the magne-  
 561 tosheath.

562 5. In the magnetosheath the distributions of the OMNI  $V_x$ ,  $V_y$  and  $V_z$  can  
 563 be compared in Figure 13d and Figure 18a, 18d, 18g, 18j; Figure 13e  
 564 and Figure 18b, 18e, 18h, 18k; furthermore in Figure 13f and Figure 18c, 18f, 18i, 18l.

565 (a) When the  $B_z$  disagrees in Figure 18a, 18b, 18c the distributions of  
 566 the OMNI  $V_x$ ,  $V_y$  and  $V_z$  are similar to the distributions of the OMNI  
 567  $V_x$ ,  $V_y$  and  $V_z$  in Figure 13d, 13e and 13f.

568 (b) When the  $V_x$  disagrees in simulations and measurements in Figure 18d, 18e, 18f  
 569 the distributions of the OMNI  $V_x$ ,  $V_y$  and  $V_z$  are similar to the dis-  
 570 tributions of the OMNI  $V_x$ ,  $V_y$  and  $V_z$  in Figure 13d, 13e and 13f.

571 (c) When the  $n_{CIS}$  disagrees in Figure 18g, 18h, 18i the distributions of  
 572 the OMNI  $V_x$ ,  $V_y$  and  $V_z$  are similar to the distributions of the OMNI  
 573  $V_x$ ,  $V_y$  and  $V_z$  in Figure 13d, 13e and 13f.

574 (d) When the  $n_{EFW}$  disagrees in simulations and measurements in Fig-  
 575 ure 18j, 18k, 18l the distributions of the OMNI  $V_x$ ,  $V_y$  and  $V_z$  are sim-  
 576 ilar to the distributions of the OMNI  $V_x$ ,  $V_y$  and  $V_z$  in Figure 13d, 13e  
 577 and 13f.

578 The distributions agree quite well because in Table 5 the number of the  
 579 poorly correlated intervals 18, 50, 33 and 30 for the  $B_z$ , the  $V_x$ , the  $n_{CIS}$   
 580 and  $n_{CIS}$  components, respectively. The number of cases are higher and  
 581 the values of the OMNI  $V_x$ ,  $V_y$  and  $V_z$  are not peculiar in the magne-  
 582 tosheath.

583 6. In the magnetosheath the distributions of the OMNI  $P$  can be compared  
 584 in Figure 13g and Figure 19a, 19b, 19c, 19d.

585 (a) When the  $B_z$  disagrees in Figure 19a the distribution of the OMNI  
 586  $P$  is similar to the distribution of the OMNI  $P$  in Figure 13g.

587 (b) When the  $V_x$  disagrees in simulations and measurements in Figure 19b  
 588 the distribution of the OMNI  $P$  is similar to the distributions of the  
 589 OMNI  $P$  in Figure 13g.

- 590       (c) When the  $n_{CIS}$  disagrees in simulations and measurements in Figure 19c  
 591           the distribution of the OMNI  $P$  is similar to the distributions of the  
 592           OMNI  $P$  in Figure 13g.
- 593       (d) When the  $n_{EFW}$  disagrees in simulations and measurements in Fig-  
 594           ure 19d the distribution of the OMNI  $P$  is similar to the distributions  
 595           of the OMNI  $P$  in Figure 13g.

596       The distributions do not agree perfectly because in Table 5 the num-  
 597           ber of the poorly correlated intervals is only 6, 12 and 9 for the  $V_x$ , the  
 598            $n_{CIS}$  and  $n_{CIS}$  components, respectively. The distributions agree quite  
 599           well because in Table 5 the number of the poorly correlated intervals  
 600           18, 50, 33 and 30 for the  $B_z$ , the  $V_x$ , the  $n_{CIS}$  and  $n_{CIS}$  components, re-  
 601           spectively. The number of cases are higher and the values of the OMNI  
 602            $P$  are not peculiar in the magnetosheath.

603       The inaccuracy of the GUMICS-4 simulations does not depend on the OMNI  
 604           parameters in the solar wind and magnetosheath regions. The same study  
 605           does not need to be done for the magnetosphere because the deviance of the  
 606           measurements and the simulations is so large that it cannot be caused by the  
 607           wrong OMNI solar wind parameters.

608       The bow shock positions agree in the GUMICS simulations and the Cluster SC3  
 609           measurements. However, the magnetopause locations do not fit well as the bow shock  
 610           in simulations and observations. In simulations the location of the magnetopause is de-  
 611           termined from peaks in currents density, particle density gradient, or changes in flow  
 612           velocity [Siscoe et al., 2001; García and Hughes, 2007; Gordeev et al., 2013, see refer-  
 613           ences therein]. In this paper the previously saved simulation parameters along the vir-  
 614           tual Cluster SC3 orbit are analysed. Therefore, the above mentioned methods cannot  
 615           be applied. The reason of the inaccuracy of the magnetopause positions in the simula-  
 616           tions must be the missing inner magnetosphere [...] module. This discrepancy of the  
 617           magnetopause location agrees with the results of Gordeev et al. [2013] and Fácskó et al.  
 618           [2016]. Gordeev et al. [2013] compared synthetic GUMICS runs with an empirical for-  
 619           mula for the magnetopause locations. Fácskó et al. [2016] used OMNI solar wind data  
 620           as input and got the same result as Gordeev et al. [2013] and this paper. Surprisingly  
 621           the neutral sheets are visible in both simulations and observations (Figure 20, Table 8).

622 This experience is exceptional because the night side magnetosphere of the GUMICS–4  
 623 simulations is small and twisted [Gordeev *et al.*, 2013; Facskó *et al.*, 2016]. However, in  
 624 these cases the IMF has no large  $B_y$  component. From Facskó *et al.* [2016] we know that  
 625 the GUMICS has normal long tail (or night side magnetosphere) if the  $B_y$  is small.

## 626 5 Summary and conclusions

627 Based on the previously created 1-year long GUMICS–4 run global MHD simu-  
 628 lation results are compared with Cluster SC3 magnetic field, solar wind velocity and den-  
 629 sity measurements along the spacecraft orbit. Intervals are selected when the Cluster SC3  
 630 and the virtual space probe are situated in the solar wind, magnetosheath and the mag-  
 631 netosphere and their correlation are calculated. Bow shock, magnetopause and neutral  
 632 sheet crossings are selected and their visibility and relative position are compared. We  
 633 achieved the following results:

- 634 1. In the solar wind the agreement of the  $B_z$ , the  $V_x$  and the  $n_{EFW}$  is very good, fur-  
     thermore the agreement of the  $n_{CIS}$  is also good.
- 635 2. In the magnetosheath the agreement of the magnetic field component, the ion plasma  
     moments and the calculated empirical density is a bit worse than in the solar wind.  
     The  $V_x$ , the  $n_{EFW}$  and the  $n_{CIS}$  fits better than the  $B_z$  component in the mag-  
     netosheath. Their agreement is still good. The reason of the deviation is the tur-  
     bulent behavior of the slowed down and thermalised turbulent solar wind.
- 636 3. In neither the dayside nor the nightside magnetosphere can the GUMICS–4 pro-  
     vide realistic results. The simulation outputs and the spacecraft measurement dis-  
     agree in this region. The reason of this deviation must be the missing coupled in-  
     ner magnetosphere model. The applied tilted dipole approach is not satisfactory  
     in the magnetosphere at all.
- 637 4. The GUMICS–4 code causes the deviations between the simulations and the space-  
     craft measurements because the upstream solar wind conditions seem to be nor-  
     mal when the disagreement of the different kinds of time series is large.
- 638 5. The position of the bow shock and the neutral sheet agrees well in the simulations  
     and the Cluster SC3 magnetic field, ion plasma moments and derived electron den-  
     sity measurements in this study. The position of the magnetopause does not fit

652 that well. The reason of this latest discrepancy must be the missing coupled in-  
 653 ner magnetosphere model too.

654 The GUMICS–4 has incredible scientific and strategic importance for the European Space  
 655 Weather and Scientific community. This code developed in the Finnish Meteorological  
 656 Institute is the most developed and tested, widely used tool for modelling the cosmic en-  
 657 viroment of the Earth in the old continent. [...] **An inner magnetosphere model should**  
 658 be two way coupled to the existing configuration of the simulation tool **to improve the**  
 659 **accuracy of the simulations.**

## 660 Acknowledgments

661 The OMNI data were obtained from the GSFC/SPDF OMNIWeb interface at <http://omniweb.gsfc.nasa.gov>.  
 662 The authors thank the FGM Team (PI: Chris Carr), the CIS Team (PI: Iannis Dandouras),  
 663 the WHISPER Team (PI: Jean-Louis Rauch), the EFW Team (PI: Mats Andre) and the  
 664 Cluster Science Archive for providing FGM magnetic field, CIS HIA ion plasma and WHIS-  
 665 PER electron density measurements. Data analysis was partly done with the QSAS sci-  
 666 ence analysis system provided by the United Kingdom Cluster Science Centre (Impe-  
 667 rial College London and Queen Mary, University of London) supported by the Science  
 668 and Technology Facilities Council (STFC). Eija Tanskanen acknowledges financial sup-  
 669 port from the Academy of Finland for the ReSoLVE Centre of Excellence (project No. 272157).  
 670 Gábor Facskó thanks Anna-Mária Vigh for improving the English of the paper. The au-  
 671 thors thank Pekka Janhunen for developing the GUMICS–4 code; furthermore Minna  
 672 Palmroth and Zoltán Vörös for the useful discussions. The work of Gábor Facskó was  
 673 supported by mission science funding for the Van Allen Probes mission, the American  
 674 Geophysical Union and the HAS Research Centre for Astronomy and Earth Sciences,  
 675 Sopron, Hungary. For further use of the year run data, [...] **request the authors or**  
 676 use the archive of the Community Coordinated Modelling Center (<https://ccmc.gsfc.nasa.gov/publications/posted>)  
 677

## 678 References

679 Balogh, A., M. W. Dunlop, S. W. H. Cowley, D. J. Southwood, J. G. Thomlinson,  
 680 K. H. Glassmeier, G. Musmann, H. Luhr, S. Buchert, M. H. Acuna, D. H. Fair-  
 681 field, J. A. Slavin, W. Riedler, K. Schwingenschuh, and M. G. Kivelson (1997),  
 682 The Cluster Magnetic Field Investigation, *Space Science Reviews*, 79, 65–91, doi:

- 683 10.1023/A:1004970907748.
- 684 Balogh, A., C. M. Carr, M. H. Acuña, M. W. Dunlop, T. J. Beek, P. Brown,  
685 K. Fornacon, E. Georgescu, K. Glassmeier, J. Harris, G. Musmann, T. Oddy, and  
686 K. Schwingenschuh (2001), The Cluster Magnetic Field Investigation: overview of  
687 in-flight performance and initial results, *Annales Geophysicae*, *19*, 1207–1217.
- 688 Bartels, J., N. H. Heck, and H. F. Johnston (1939), The three-hour-range index mea-  
689 suring geomagnetic activity, *Terrestrial Magnetism and Atmospheric Electricity*  
690 (*Journal of Geophysical Research*), *44*, 411, doi:10.1029/TE044i004p00411.
- 691 Blagau, A., I. Dandouras, A. Barthe, S. Brunato, G. Facskó, and V. Constanti-  
692 nescu (2013), In-flight calibration of Hot Ion Analyser onboard Cluster, *Geo-  
693 scientific Instrumentation, Methods and Data Systems Discussions*, *3*, 407–435,  
694 doi:10.5194/gid-3-407-2013.
- 695 Blagau, A., I. Dandouras, A. Barthe, S. Brunato, G. Facskó, and V. Constantinescu  
696 (2014), In-flight calibration of the Hot Ion Analyser on board Cluster, *Geoscientific  
697 Instrumentation, Methods and Data Systems*, *3*, 49–58, doi:10.5194/gi-3-49-  
698 2014.
- 699 Chittenden, J. P., S. V. Lebedev, C. A. Jennings, S. N. Bland , and A. Ciardi  
700 (2004), X-ray generation mechanisms in three-dimensional simulations of wire  
701 array Z-pinches, *Plasma Physics and Controlled Fusion*, *46*(12B), B457–B476,  
702 doi:10.1088/0741-3335/46/12B/039.
- 703 Ciardi, A., S. V. Lebedev, A. Frank, E. G. Blackman, J. P. Chittenden, C. J. Jen-  
704 nings, D. J. Ampleford, S. N. Bland, S. C. Bott, J. Rapley, G. N. Hall, F. A.  
705 Suzuki-Vidal, A. Marocchino, T. Lery, and C. Stehle (2007), The evolution of  
706 magnetic tower jets in the laboratory, *Physics of Plasmas*, *14*(5), 056,501–056,501,  
707 doi:10.1063/1.2436479.
- 708 Credland, J., G. Mecke, and J. Ellwood (1997), The Cluster Mission: ESA'S  
709 Spacefleet to the Magnetosphere, *Space Science Reviews*, *79*, 33–64, doi:  
710 10.1023/A:1004914822769.
- 711 Davis, T. N., and M. Sugiura (1966), Auroral electrojet activity index AE and its  
712 universal time variations, *Journal of Geophysical Research*, *71*, 785–801, doi:  
713 10.1029/JZ071i003p00785.
- 714 Décréau, P. M. E., P. Fergeau, V. Krasnoselskikh, E. Le Guiriec, M. Lévéque,  
715 P. Martin, O. Randriamboarison, J. L. Rauch, F. X. Sené, H. C. Séran, J. G.

- 716 Trotignon, P. Canu, N. Cornilleau, H. de Féraudy, H. Alleyne, K. Yearby, P. B.  
717 Mögensen, G. Gustafsson, M. André, D. C. Gurnett, F. Darrouzet, J. Lemaire,  
718 C. C. Harvey, P. Travnicek, and Whisper Experimenters Group (2001), Early re-  
719 sults from the Whisper instrument on Cluster: an overview, *Annales Geophysicae*,  
720 *19*, 1241–1258, doi:10.5194/angeo-19-1241-2001.
- 721 Escoubet, C. P., M. Fehringer, and M. Goldstein (2001), Introduction The Cluster  
722 mission, *Annales Geophysicae*, *19*, 1197–1200, doi:10.5194/angeo-19-1197-2001.
- 723 Facskó, G., I. Honkonen, T. Živković, L. Palin, E. Kallio, K. Ågren, H. Opgenoorth,  
724 E. I. Tanskanen, and S. Milan (2016), One year in the Earth’s magnetosphere: A  
725 global MHD simulation and spacecraft measurements, *Space Weather*, *14*, 351–  
726 367, doi:10.1002/2015SW001355.
- 727 Facskó, G., T. B. Balogh, E. I. Anekallu, C. R. and Tanskanen, P. Peitso, L. Degener,  
728 M. Kangwa, T. Laitinen, and S. Laakso, H. Burley (in preparation), Bow shock  
729 identification in cluster measurements, *Space Weather*.
- 730 Fazakerley, A. N., A. D. Lahiff, R. J. Wilson, I. Rozum, C. Anekallu, M. West, and  
731 H. Bacai (2010a), PEACE Data in the Cluster Active Archive, *Astrophysics and  
732 Space Science Proceedings*, *11*, 129–144, doi:10.1007/978-90-481-3499-1\_8.
- 733 Fazakerley, A. N., A. D. Lahiff, I. Rozum, D. Kataria, H. Bacai, C. Anekallu,  
734 M. West, and A. Åsnes (2010b), Cluster-PEACE In-flight Calibration Status,  
735 *Astrophysics and Space Science Proceedings*, *11*, 281–299, doi:10.1007/978-90-481-  
736 3499-1\_19.
- 737 García, K. S., and W. J. Hughes (2007), Finding the Lyon-Fedder-Mobarry mag-  
738 netopause: A statistical perspective, *Journal of Geophysical Research (Space  
739 Physics)*, *112*(A6), A06229, doi:10.1029/2006JA012039.
- 740 Gordeev, E., G. Facskó, V. Sergeev, I. Honkonen, M. Palmroth, P. Janhunen, and  
741 S. Milan (2013), Verification of the GUMICS-4 global MHD code using empirical  
742 relationships, *Journal of Geophysical Research (Space Physics)*, *118*, 3138–3146,  
743 doi:10.1002/jgra.50359.
- 744 Greenwald, R. A., K. B. Baker, J. R. Dudeney, M. Pincock, T. B. Jones, E. C.  
745 Thomas, J.-P. Villain, J.-C. Cerisier, C. Senior, C. Hanuise, R. D. Hunsucker,  
746 G. Sofko, J. Koehler, E. Nielsen, R. Pellinen, A. D. M. Walker, N. Sato,  
747 and H. Yamagishi (1995), Darn/Superdarn: A Global View of the Dynam-  
748 ics of High-Latitude Convection, *Space Science Reviews*, *71*, 761–796, doi:

- 749 10.1007/BF00751350.
- 750 Guild, T. B., H. E. Spence, E. L. Kepko, V. Merkin, J. G. Lyon, M. Wiltberger, and  
751 C. C. Goodrich (2008a), Geotail and LFM comparisons of plasma sheet clima-  
752 tology: 1. Average values, *Journal of Geophysical Research (Space Physics)*, 113,  
753 A04216, doi:10.1029/2007JA012611.
- 754 Guild, T. B., H. E. Spence, E. L. Kepko, V. Merkin, J. G. Lyon, M. Wiltberger, and  
755 C. C. Goodrich (2008b), Geotail and LFM comparisons of plasma sheet climatol-  
756 ogy: 2. Flow variability, *Journal of Geophysical Research (Space Physics)*, 113,  
757 A04217, doi:10.1029/2007JA012613.
- 758 Gustafsson, G., R. Bostrom, B. Holback, G. Holmgren, A. Lundgren, K. Stasiewicz,  
759 L. Ahlen, F. S. Mozer, D. Pankow, P. Harvey, P. Berg, R. Ulrich, A. Pedersen,  
760 R. Schmidt, A. Butler, A. W. C. Fransen, D. Klinge, M. Thomsen, C.-G. Faltham-  
761 mar, P.-A. Lindqvist, S. Christenson, J. Holtet, B. Lybekk, T. A. Sten, P. Tan-  
762 skanen, K. Lappalainen, and J. Wygant (1997), The Electric Field and Wave  
763 Experiment for the Cluster Mission, *Space Science Reviews*, 79, 137–156, doi:  
764 10.1023/A:1004975108657.
- 765 Gustafsson, G., M. André, T. Carozzi, A. I. Eriksson, C.-G. Fälthammar, R. Grard,  
766 G. Holmgren, J. A. Holtet, N. Ivchenko, T. Karlsson, Y. Khotyaintsev, S. Klimov,  
767 H. Laakso, P.-A. Lindqvist, B. Lybekk, G. Marklund, F. Mozer, K. Mursula,  
768 A. Pedersen, B. Popielawska, S. Savin, K. Stasiewicz, P. Tanskanen, A. Vaivads,  
769 and J.-E. Wahlund (2001), First results of electric field and density observations  
770 by Cluster EFW based on initial months of operation, *Annales Geophysicae*, 19,  
771 1219–1240, doi:10.5194/angeo-19-1219-2001.
- 772 Haiducek, J. D., D. T. Welling, N. Y. Ganushkina, S. K. Morley, and D. S. Oz-  
773 turk (2017), SWMF Global Magnetosphere Simulations of January 2005: Geo-  
774 magnetic Indices and Cross-Polar Cap Potential, *Space Weather*, 15, 1567–1587,  
775 doi:10.1002/2017SW001695.
- 776 Iyemori, T. (1990), Storm-time magnetospheric currents inferred from mid-latitude  
777 geomagnetic field variations, *Journal of Geomagnetism and Geoelectricity*, 42,  
778 1249–1265, doi:10.5636/jgg.42.1249.
- 779 Janhunen, P., M. Palmroth, T. Laitinen, I. Honkonen, L. Juusola, G. Facskó, and  
780 T. I. Pulkkinen (2012), The GUMICS-4 global MHD magnetosphere-ionosphere  
781 coupling simulation, *Journal of Atmospheric and Solar-Terrestrial Physics*, 80,

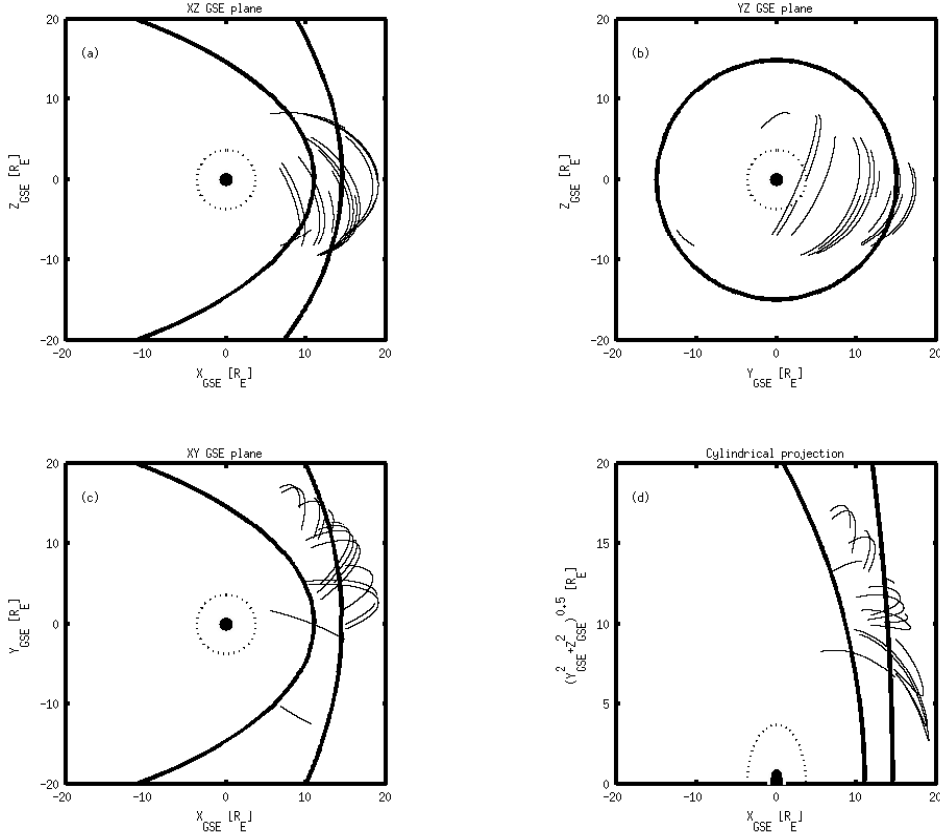
- 782 48–59, doi:10.1016/j.jastp.2012.03.006.
- 783 Johnstone, A. D., C. Alsop, S. Burge, P. J. Carter, A. J. Coates, A. J. Coker, A. N.  
784 Fazakerley, M. Grande, R. A. Gowen, C. Gurgiolo, B. K. Hancock, B. Narheim,  
785 A. Preece, P. H. Sheather, J. D. Winningham, and R. D. Woodliffe (1997), Peace:  
786 a Plasma Electron and Current Experiment, *Space Science Reviews*, 79, 351–398,  
787 doi:10.1023/A:1004938001388.
- 788 Juusola, L., O. Amm, K. Kauristie, and A. Viljanen (2007), A model for estimating  
789 the relation between the Hall to Pedersen conductance ratio and ground magnetic  
790 data derived from CHAMP satellite statistics, *Annales Geophysicae*, 25, 721–736,  
791 doi:10.5194/angeo-25-721-2007.
- 792 Juusola, L., G. Facskó, I. Honkonen, P. Janhunen, H. Vanhamäki, K. Kauristie,  
793 T. V. Laitinen, S. E. Milan, M. Palmroth, E. I. Tanskanen, and A. Viljanen  
794 (2014), Statistical comparison of seasonal variations in the GUMICS-4 global  
795 MHD model ionosphere and measurements, *Space Weather*, 12, 582–600, doi:  
796 10.1002/2014SW001082.
- 797 Kallio, E., and G. Facskó (2015), Properties of plasma near the moon in the magne-  
798 totail, *Planetary and Space Science*, 115, 69–76, doi:10.1016/j.pss.2014.11.007.
- 799 Kokubun, S., T. Yamamoto, M. H. Acuña, K. Hayashi, K. Shiokawa, and H. Kawano  
800 (1994), The GEOTAIL Magnetic Field Experiment., *Journal of Geomagnetism*  
801 and *Geoelectricity*, 46, 7–21, doi:10.5636/jgg.46.7.
- 802 Lakka, A., T. I. Pulkkinen, A. P. Dimmock, M. Myllys, I. Honkonen, and M. Palm-  
803 roth (2018a), The Cross-Polar Cap Saturation in GUMICS-4 During High Solar  
804 Wind Driving, *Journal of Geophysical Research (Space Physics)*, 123, 3320–3332,  
805 doi:10.1002/2017JA025054.
- 806 Lakka, A., T. I. Pulkkinen, A. P. Dimmock, E. Kilpua, M. Ala-Lahti, I. Honko-  
807 nen, M. Palmroth, and Raukunen (2018b), Icme impact at earth with low and  
808 typical mach number plasma characteristics, *Annales Geophysicae Discussions*,  
809 <https://doi.org/10.5194/angeo-2018-81>.
- 810 Lani, A., A. Sanna, N. Villedieu, and M. Panesi (2012), COOLFluiD an Open Com-  
811 putational Platform for Aerothermodynamics and Flow-Radiation Coupling, in  
812 *ESA Special Publication*, *ESA Special Publication*, vol. 714, p. 45.
- 813 Lyon, J. G., J. A. Fedder, and C. M. Mobarry (2004), The Lyon-Fedder-Mobarry  
814 (LFM) global MHD magnetospheric simulation code, *Journal of Atmospheric and*

- 815        *Solar-Terrestrial Physics*, 66, 1333–1350, doi:10.1016/j.jastp.2004.03.020.
- 816        Mejnertsen, L., J. P. Eastwood, J. P. Chittenden, and A. Masters (2016), Global  
817        MHD simulations of Neptune's magnetosphere, *Journal of Geophysical Research  
818        (Space Physics)*, 121(8), 7497–7513, doi:10.1002/2015JA022272.
- 819        Mejnertsen, L., J. P. Eastwood, H. Hietala, S. J. Schwartz, and J. P. Chittenden  
820        (2018), Global MHD Simulations of the Earth's Bow Shock Shape and Motion  
821        Under Variable Solar Wind Conditions, *Journal of Geophysical Research (Space  
822        Physics)*, 123(1), 259–271, doi:10.1002/2017JA024690.
- 823        Mukai, T., S. Machida, Y. Saito, M. Hirahara, T. Terasawa, N. Kaya, T. Obara,  
824        M. Ejiri, and A. Nishida (1994), The Low Energy Particle (LEP) Experiment on-  
825        board the GEOTAIL Satellite., *Journal of Geomagnetism and Geoelectricity*, 46,  
826        669–692, doi:10.5636/jgg.46.669.
- 827        Peredo, M., J. A. Slavin, E. Mazur, and S. A. Curtis (1995), Three-dimensional po-  
828        sition and shape of the bow shock and their variation with Alfvénic, sonic and  
829        magnetosonic Mach numbers and interplanetary magnetic field orientation, *Jour-  
830        nal of Geophysical Research*, 100, 7907–7916, doi:10.1029/94JA02545.
- 831        Poedts, S., A. Kochanov, A. Lani, C. Scolini, C. Verbeke, S. Hosteaux, E. Chané,  
832        H. Deconinck, N. Mihalache, F. Diet, D. Heynderickx, J. De Keyser, E. De  
833        Donder, N. B. Crosby, M. Echim, L. Rodriguez, R. Vansintjan, F. Verstringe,  
834        B. Mampaey, R. Horne, S. Glauert, P. Jiggens, R. Keil, A. Glover, G. Deprez, and  
835        J.-P. Luntama (2020), The Virtual Space Weather Modelling Centre, *Journal of  
836        Space Weather and Space Climate*, 10, 14, doi:10.1051/swsc/2020012.
- 837        Powell, K. G., P. L. Roe, T. J. Linde, T. I. Gombosi, and D. L. De Zeeuw (1999), A  
838        Solution-Adaptive Upwind Scheme for Ideal Magnetohydrodynamics, *Journal of  
839        Computational Physics*, 154, 284–309, doi:10.1006/jcph.1999.6299.
- 840        Raeder, J., D. Larson, W. Li, E. L. Kepko, and T. Fuller-Rowell (2008), OpenG-  
841        GCM Simulations for the THEMIS Mission, *Space Science Reviews*, 141, 535–555,  
842        doi:10.1007/s11214-008-9421-5.
- 843        Reigber, C., H. Lühr, and P. Schwintzer (2002), CHAMP mission status, *Advances  
844        in Space Research*, 30, 129–134, doi:10.1016/S0273-1177(02)00276-4.
- 845        Reme, H., J. M. Bosqued, J. A. Sauvaud, A. Cros, J. Dandouras, C. Aoustin,  
846        J. Bouyssou, T. Camus, J. Cuvilo, C. Martz, J. L. Medale, H. Perrier, D. Rome-  
847        fort, J. Rouzaud, C. D'Uston, E. Mobius, K. Crocker, M. Granoff, L. M. Kistler,

- 848 M. Popecki, D. Hovestadt, B. Klecker, G. Paschmann, M. Scholer, C. W. Carl-  
 849 son, D. W. Curtis, R. P. Lin, J. P. McFadden, V. Formisano, E. Amata, M. B.  
 850 Bavassano-Cattaneo, P. Baldetti, G. Belluci, R. Bruno, G. Chionchio, A. di Lel-  
 851 lis, E. G. Shelley, A. G. Ghielmetti, W. Lennartsson, A. Korth, H. Rosenbauer,  
 852 R. Lundin, S. Olsen, G. K. Parks, M. McCarthy, and H. Balsiger (1997), The  
 853 Cluster Ion Spectrometry (CIS) Experiment, *Space Science Reviews*, 79, 303–350,  
 854 doi:10.1023/A:1004929816409.
- 855 Rème, H., C. Aoustin, J. M. Bosqued, I. Dandouras, B. Lavraud, J. A. Sauvaud,  
 856 A. Barthe, J. Bouyssou, T. Camus, O. Coeur-Joly, A. Cros, J. Cuval, F. Ducay,  
 857 Y. Garbarowitz, J. L. Medale, E. Penou, H. Perrier, D. Romefort, J. Rouzaud,  
 858 C. Vallat, D. Alcaydé, C. Jacquay, C. Mazelle, C. D'Uston, E. Möbius, L. M.  
 859 Kistler, K. Crocker, M. Granoff, C. Mouikis, M. Popecki, M. Vosbury, B. Klecker,  
 860 D. Hovestadt, H. Kucharek, E. Kuenneth, G. Paschmann, M. Scholer, N. Sckopke,  
 861 E. Seidenschwang, C. W. Carlson, D. W. Curtis, C. Ingraham, R. P. Lin, J. P.  
 862 McFadden, G. K. Parks, T. Phan, V. Formisano, E. Amata, M. B. Bavassano-  
 863 Cattaneo, P. Baldetti, R. Bruno, G. Chionchio, A. di Lellis, M. F. Marcucci,  
 864 G. Pallocchia, A. Korth, P. W. Daly, B. Graeve, H. Rosenbauer, V. Vasyliunas,  
 865 M. McCarthy, M. Wilber, L. Eliasson, R. Lundin, S. Olsen, E. G. Shelley, S. Fuseli-  
 866 ler, A. G. Ghielmetti, W. Lennartsson, C. P. Escoubet, H. Balsiger, R. Friedel, J.-  
 867 B. Cao, R. A. Kovrashkin, I. Papamastorakis, R. Pellat, J. Scudder, and B. Son-  
 868 nerup (2001), First multispacecraft ion measurements in and near the Earth's  
 869 magnetosphere with the identical Cluster ion spectrometry (CIS) experiment,  
 870 *Annales Geophysicae*, 19, 1303–1354, doi:10.5194/angeo-19-1303-2001.
- 871 Ritter, P., H. Lühr, A. Viljanen, O. Amm, A. Pulkkinen, and I. Sillanpää (2004),  
 872 Ionospheric currents estimated simultaneously from CHAMP satellite and IMAGE  
 873 ground-based magnetic field measurements: a statistical study at auroral latitudes,  
 874 *Annales Geophysicae*, 22, 417–430, doi:10.5194/angeo-22-417-2004.
- 875 Rostoker, G. (1972), Geomagnetic indices., *Reviews of Geophysics and Space  
 876 Physics*, 10, 935–950, doi:10.1029/RG010i004p00935.
- 877 Siscoe, G. L., G. M. Erickson, B. U. Sonnerup, N. C. Maynard, J. A. Schoendorf,  
 878 K. D. Siebert, D. R. Weimer, W. W. White, and G. R. Wilson (2001), The Mag-  
 879 netospheric Fluopause, in *AGU Spring Meeting Abstracts*, vol. 2001, pp. SM52D–  
 880 02.

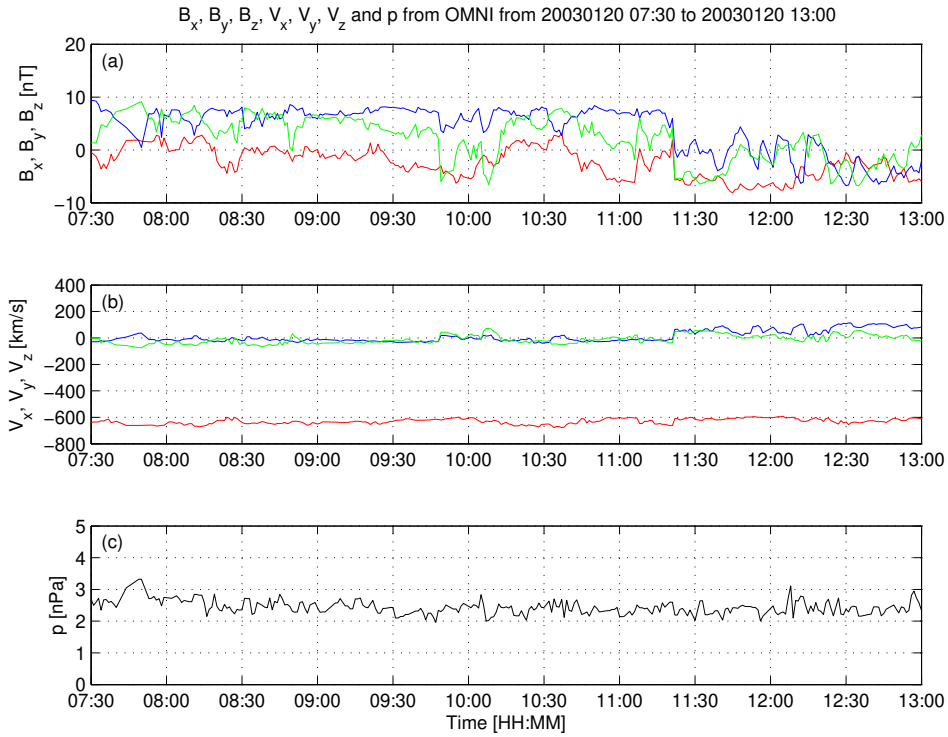
- 881 Sofko, G. J., R. Greenwald, and W. Bristow (1995), Direct determination of large-  
882 scale magnetospheric field-aligned currents with SuperDARN, *Geophysical Re-*  
883 *search Letters*, 22, 2041–2044, doi:10.1029/95GL01317.
- 884 Thomsen, M. F. (2004), Why K<sub>p</sub> is such a good measure of magnetospheric convec-  
885 tion, *Space Weather*, 2, S11004, doi:10.1029/2004SW000089.
- 886 Tóth, G., I. V. Sokolov, T. I. Gombosi, D. R. Chesney, C. R. Clauer, D. L. de  
887 Zeeuw, K. C. Hansen, K. J. Kane, W. B. Manchester, R. C. Oehmke, K. G. Pow-  
888 ell, A. J. Ridley, I. I. Roussev, Q. F. Stout, O. Volberg, R. A. Wolf, S. Sazykin,  
889 A. Chan, B. Yu, and J. Kóta (2005), Space Weather Modeling Framework: A  
890 new tool for the space science community, *Journal of Geophysical Research (Space*  
891 *Physics)*, 110, A12226, doi:10.1029/2005JA011126.
- 892 Tóth, G., B. van der Holst, I. V. Sokolov, D. L. De Zeeuw, T. I. Gombosi, F. Fang,  
893 W. B. Manchester, X. Meng, D. Najib, K. G. Powell, Q. F. Stout, A. Glo-  
894 cer, Y.-J. Ma, and M. Opher (2012), Adaptive numerical algorithms in space  
895 weather modeling, *Journal of Computational Physics*, 231, 870–903, doi:  
896 10.1016/j.jcp.2011.02.006.
- 897 Trotignon, J. G., P. M. E. Décréau, J. L. Rauch, X. Vallières, A. Rochel,  
898 S. Kouglénou, G. Lointier, G. Facskó, P. Canu, F. Darrouzet, and A. Masson  
899 (2010), The WHISPER Relaxation Sounder and the CLUSTER Active Archive,  
900 *Astrophysics and Space Science Proceedings*, 11, 185–208, doi:10.1007/978-90-481-  
901 3499-1\_12.
- 902 Trotignon, J.-G., Vallières, and the WHISPER team (2011), Calibration report of  
903 the whisper measurements in the cluster active archive (caa), *Tech. rep.*, LPC2E  
904 CNRS, caa-est-cr-whi.
- 905 Tsyganenko, N. A. (1995), Modeling the Earth's magnetospheric magnetic field  
906 confined within a realistic magnetopause, *Journal of Geophysical Research*, 100,  
907 5599–5612, doi:10.1029/94JA03193.
- 908 Vörös, Z., G. Facskó, M. Khodachenko, I. Honkonen, P. Janhunen, and M. Palmroth  
909 (2014), Windsock memory COnditioned RAM (CO-RAM) pressure effect: Forced  
910 reconnection in the Earth's magnetotail, *Journal of Geophysical Research (Space*  
911 *Physics)*, 119, 6273–6293, doi:10.1002/2014JA019857.
- 912 Wang, Z.-D., and R. L. Xu (1994), Signatures of the magnetotail neutral sheet,  
913 *Geophysical Research Letters*, 21(19), 2087–2090, doi:10.1029/94GL01960.

- 914 Weimer, D. R. (2005), Improved ionospheric electrodynamic models and applica-  
915 tion to calculating Joule heating rates, *Journal of Geophysical Research (Space*  
916 *Physics)*, 110, A05306, doi:10.1029/2004JA010884.
- 917 Wiltberger, M., E. J. Rigler, V. Merkin, and J. G. Lyon (2017), Structure of High  
918 Latitude Currents in Magnetosphere-Ionosphere Models, *Space Science Reviews*,  
919 206, 575–598, doi:10.1007/s11214-016-0271-2.
- 920 Zhang, B., W. Lotko, M. J. Wiltberger, O. J. Brambles, and P. A. Damiano (2011),  
921 A statistical study of magnetosphere-ionosphere coupling in the Lyon-Fedder-  
922 Mobarry global MHD model, *Journal of Atmospheric and Solar-Terrestrial  
923 Physics*, 73, 686–702, doi:10.1016/j.jastp.2010.09.027.
- 924 Zhang, B., K. A. Sorathia, J. G. Lyon, V. G. Merkin, J. S. Garretson, and M. Wilt-  
925 berger (2019), GAMERA: A Three-dimensional Finite-volume MHD Solver for  
926 Non-orthogonal Curvilinear Geometries, *The Astrophysical Journal Supplement  
927 Series*, 244(1), 20, doi:10.3847/1538-4365/ab3a4c.

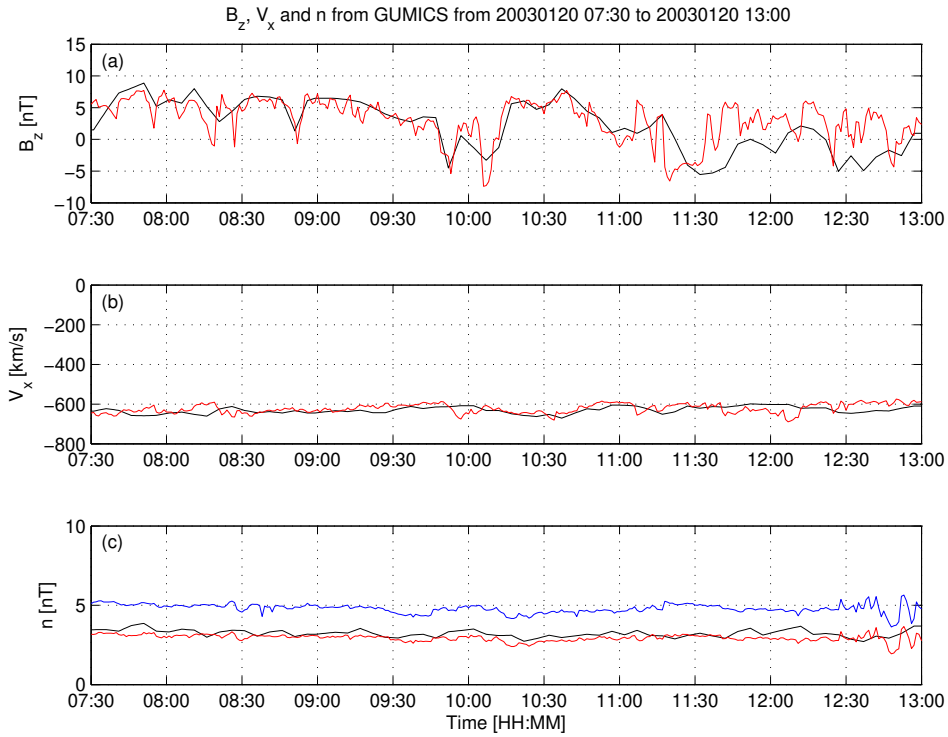


928 **Figure 1.** Cluster SC3 orbit in the solar wind in GSE system for all intervals (see Table 1).

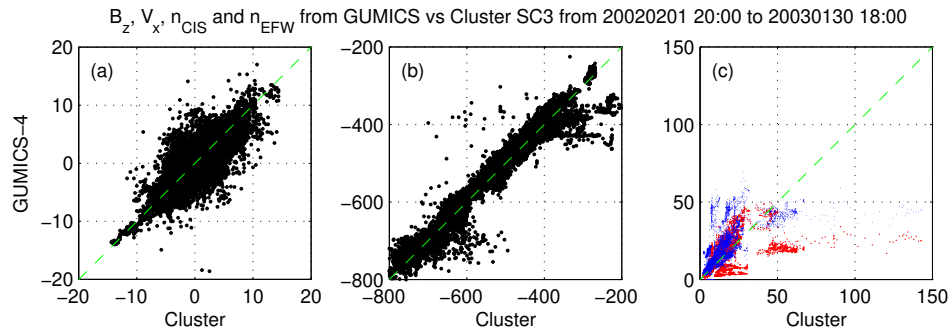
929 (a) XZ (b) YZ (c) XY (d) Cylindrical projection. Average bow-shock and magnetopause posi-  
 930 tions are drawn on all plots using solid line [Perego *et al.*, 1995; Tsyganenko, 1995, respectively].  
 931 The black dots at  $3.7 R_E$  show the boundary of the GUMICS-4 inner magnetospheric domain.  
 932 The black circle in the origo of all plots shows the size of the Earth.



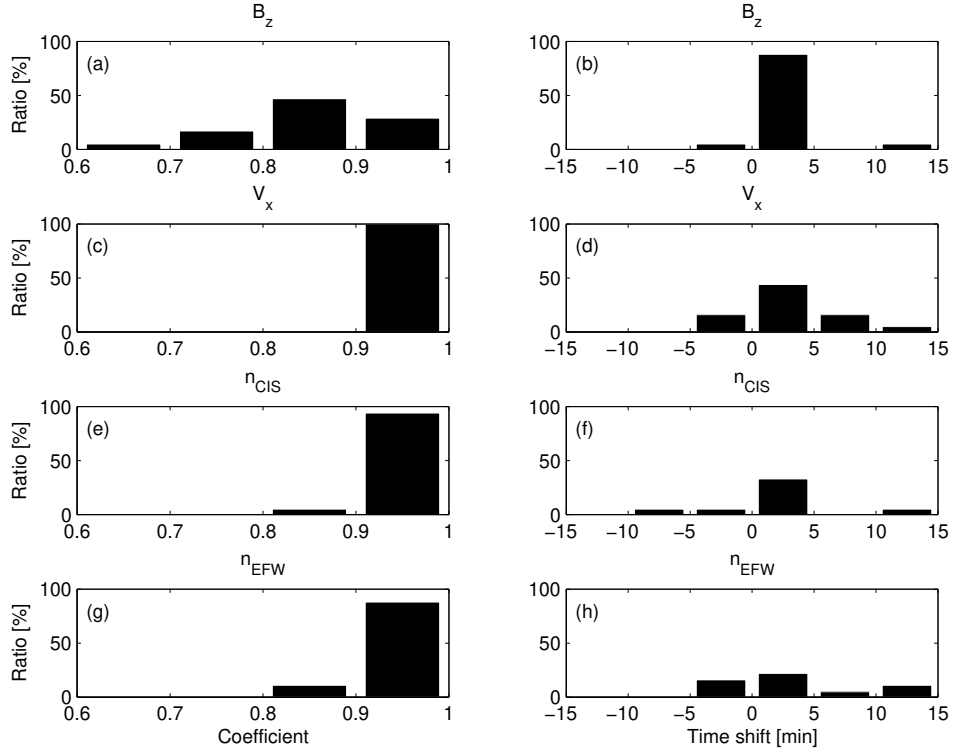
933 **Figure 2.** OMNI solar wind data in GSE system from 7:30 to 13:00 (UT) on January 20,  
934 2003. (a) Magnetic field  $B_x$  (red),  $B_y$  (green) and  $B_z$  (blue) components. (b) Solar wind velocity  
935  $V_x$  (red),  $V_y$  (green) and  $V_z$  (blue) components. (c) The  $P$  pressure of the solar wind (black).



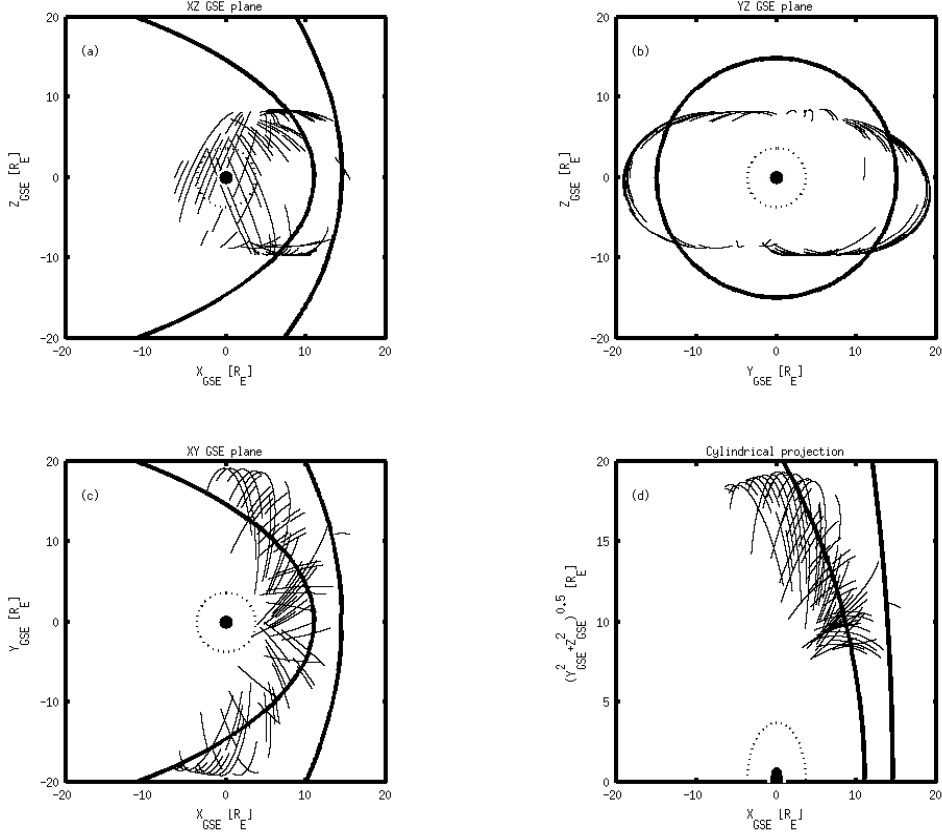
936      **Figure 3.** GUMICS-4 simulation results (black) and Cluster SC3 magnetic field Z component,  
937      ion plasma moments (red) and electron density calculated from spacecraft potential (blue) from  
938      January 20, 2003 from 7:30 to 13:00 (UT) in the solar wind in GSE system. (a) Magnetic field Z  
939      component. (b) Solar wind velocity X component (c) Solar wind density.



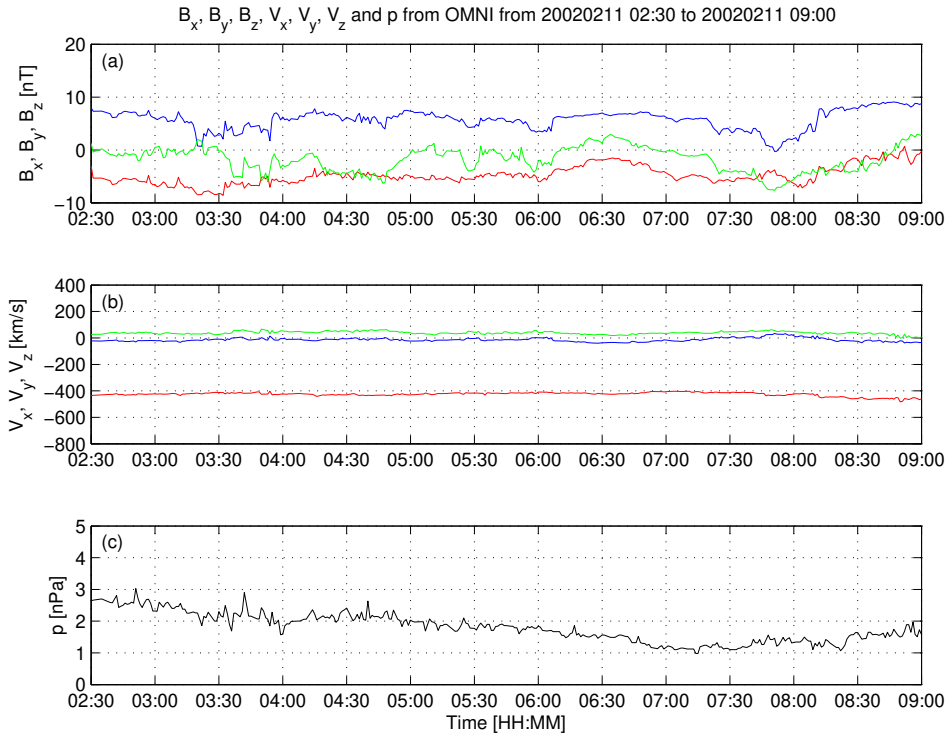
940 **Figure 4.** Scattered plots of the Cluster SC3 and GUMICS-4 simulations for all intervals in  
 941 the solar wind. The dashed line is the  $y=x$  line. (a) Magnetic field Z component in GSE system.  
 942 (b) Solar wind velocity X component in GSE system. (c) Solar wind density measured by the  
 943 CIS HIA instrument (red) and calculated from the spacecraft potential (blue).



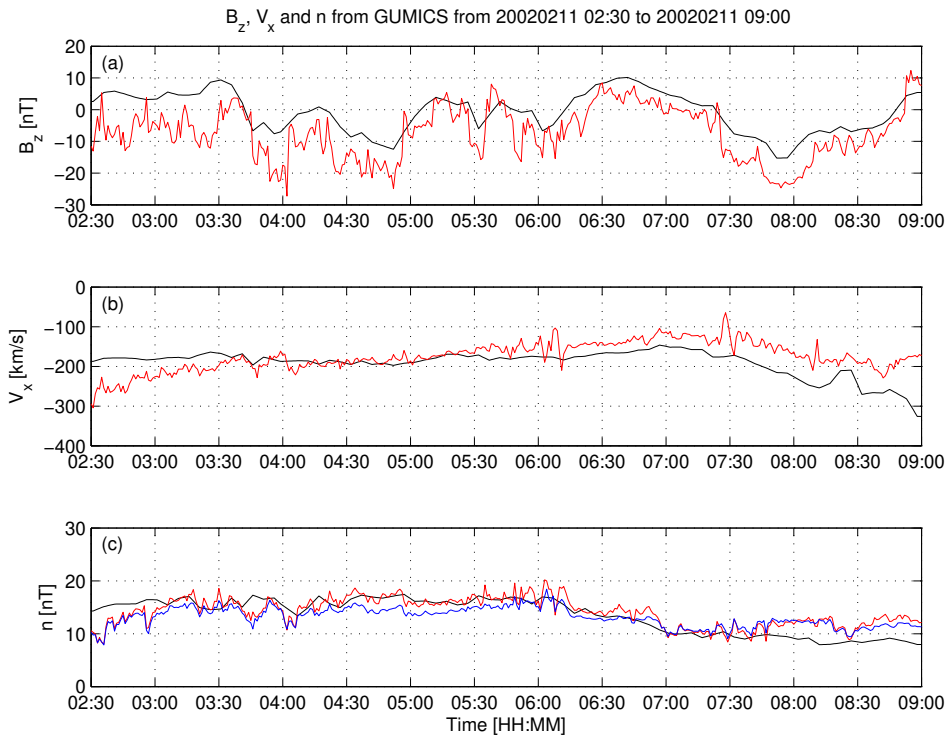
944 **Figure 5.** The distributions of the correlation coefficients (a, c, e, g) of the magnetic field Z  
 945 component ( $B_z$ ) in GSE system, solar wind velocity X component ( $V_x$ ) in GSE system, the solar  
 946 wind density measured by the CIS HIA ( $n_{CIS}$ ) instrument and calculated from the spacecraft  
 947 potential ( $n_{EFW}$ ), respectively, for all intervals in the solar wind. The distributions of the time  
 948 shifts (b, d, f, h) of the  $B_z$ , the  $V_x$ , the  $n_{CIS}$  and the  $n_{EFW}$ , respectively, for all intervals in the  
 949 solar wind.



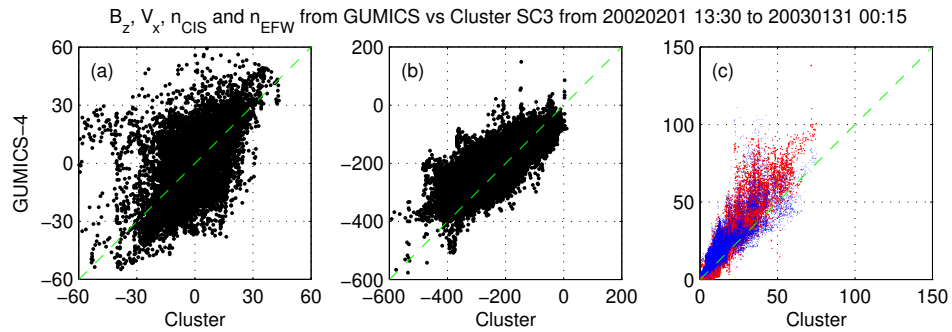
950      **Figure 6.** Cluster SC3 orbit in the magnetosheath in GSE system for all intervals (see Ta-  
 951      ble 2). (a) XZ (b) YZ (c) XY (d) Cylindrical projection. Average bow-shock and magnetopause  
 952      positions are drawn on all plots using solid line [Peredo *et al.*, 1995; Tsyganenko, 1995, respec-  
 953      tively]. The black dots at  $3.7 R_E$  show the boundary of the GUMICS-4 inner magnetospheric  
 954      domain. The black circle in the origo of all plots shows the size of the Earth.



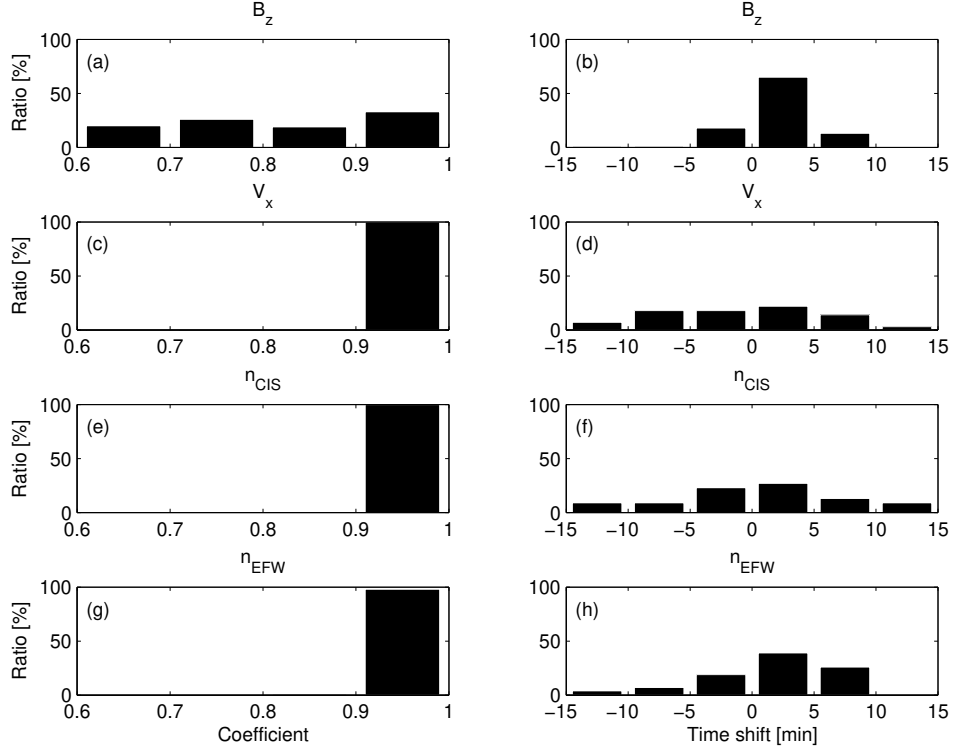
955      **Figure 7.** OMNI solar wind data in GSE system from 2:30 to 09:00 (UT) on February 11,  
956      2002. (a) Magnetic field  $B_x$  (red),  $B_y$  (green) and  $B_z$  (blue) components. (b) Solar wind velocity  
957       $V_x$  (red),  $V_y$  (green) and  $V_z$  (blue) components. (c) The  $P$  pressure of the solar wind (black).



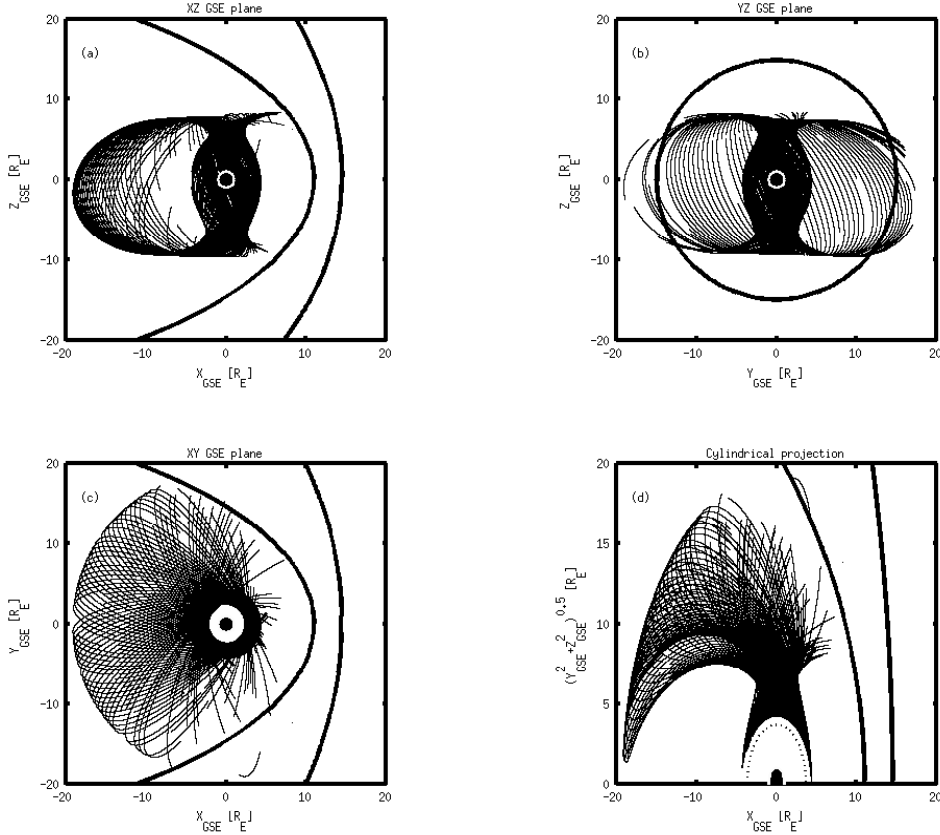
958 **Figure 8.** GUMICS-4 simulation results (black) and Cluster SC3 magnetic field Z component,  
 959 ion plasma moments (red) and electron density calculated from spacecraft potential (blue) from  
 960 February 11, 2002 from 2:30 to 9:00 (UT) in the magnetosheath in GSE system (a) Magnetic  
 961 field Z component. (b) Solar wind velocity X component (c) Solar wind density.



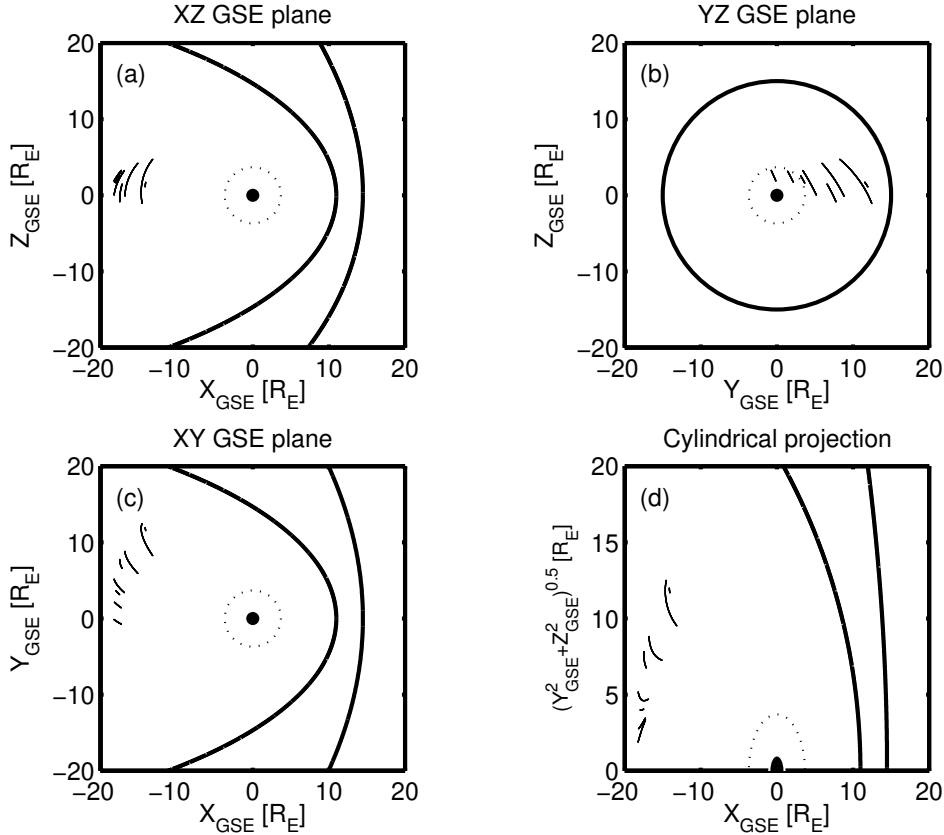
962 **Figure 9.** Scattered plots of the Cluster SC3 and GUMICS-4 simulations for all intervals in  
 963 the magnetosheath in GSE system. The dashed line is the  $y=x$  line. (a) Magnetic field Z com-  
 964 ponent. (b) Solar wind velocity X component. (c) Solar wind density measured by the CIS HIA  
 965 instrument (red) and calculated from the spacecraft potential (blue).



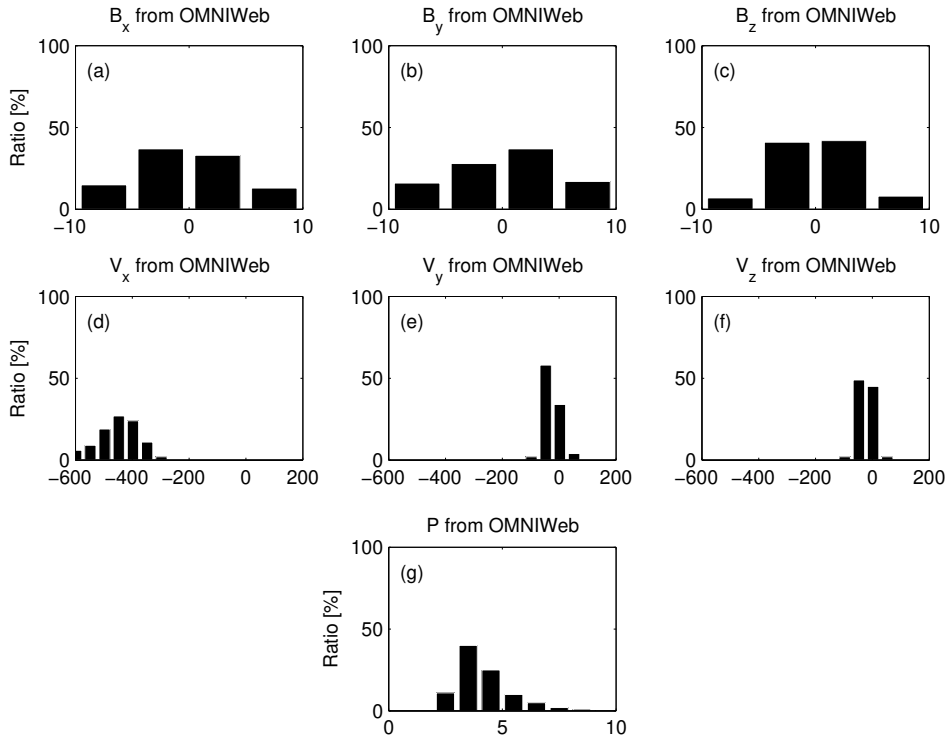
966      **Figure 10.** The distributions of the correlation coefficients (a, c, e, g) of the magnetic field Z  
 967      component ( $B_z$ ) in GSE system, solar wind velocity X component ( $V_X$ ) in GSE system, the solar  
 968      wind density measured by the CIS HIA ( $n_{CIS}$ ) instrument and calculated from the spacecraft  
 969      potential ( $n_{EFW}$ ), respectively, for all intervals in the magnetosheath. The distributions of the  
 970      time shifts (b, d, f, h) of the  $B_z$ , the  $V_X$ , the  $n_{CIS}$  and the  $n_{EFW}$ ), respectively, for all intervals  
 971      in the magnetosheath.



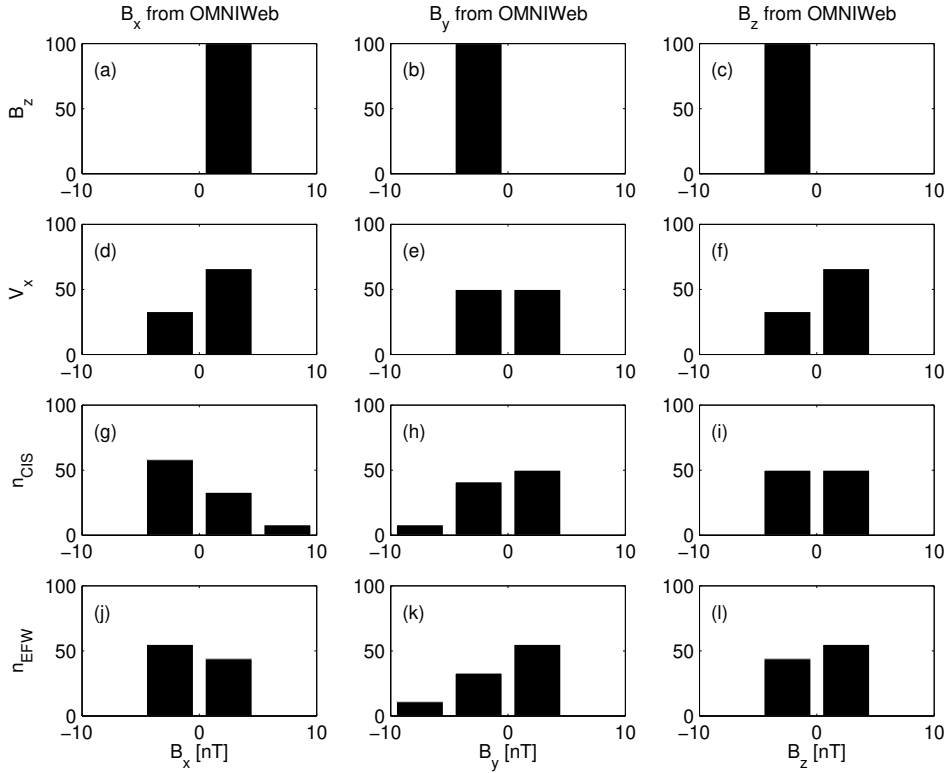
972      **Figure 11.** Cluster SC3 orbit in the magnetosphere in GSE system for all intervals (see Ta-  
 973      ble 3). (a) XZ (b) YZ (c) XY (d) Cylindrical projection. Average bow-shock and magnetopause  
 974      positions are drawn on all plots using solid line [Peredo *et al.*, 1995; Tsyganenko, 1995, respec-  
 975      tively]. The black dots at  $3.7 R_E$  show the boundary of the GUMICS-4 inner magnetospheric  
 976      domain. The black circle in the origo of all plots shows the size of the Earth.



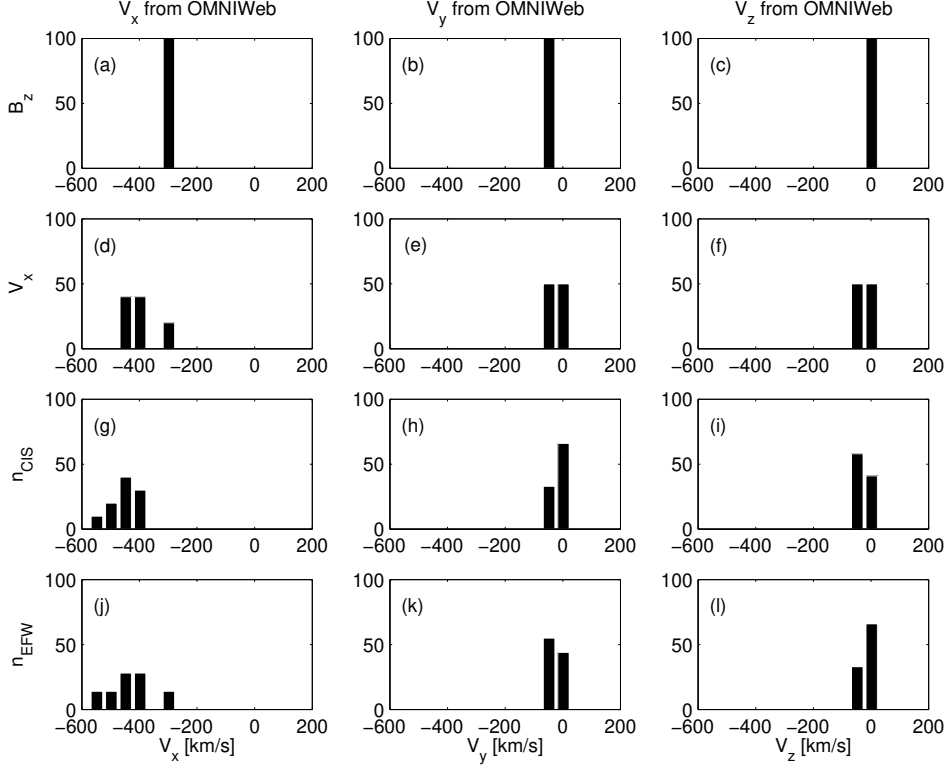
977 **Figure 12.** Cluster SC3 orbit in the tail in GSE system for all intervals (see Table 8). (a)  
 978 (b) (c) (d) Cylindrical projection. Average bow-shock and magnetopause positions  
 979 are drawn on all plots using solid line [Perego *et al.*, 1995; Tsyganenko, 1995, respectively]. The  
 980 black dots at  $3.7 R_E$  show the boundary of the GUMICS-4 inner magnetospheric domain. The  
 981 black circle in the origo of all plots shows the size of the Earth.



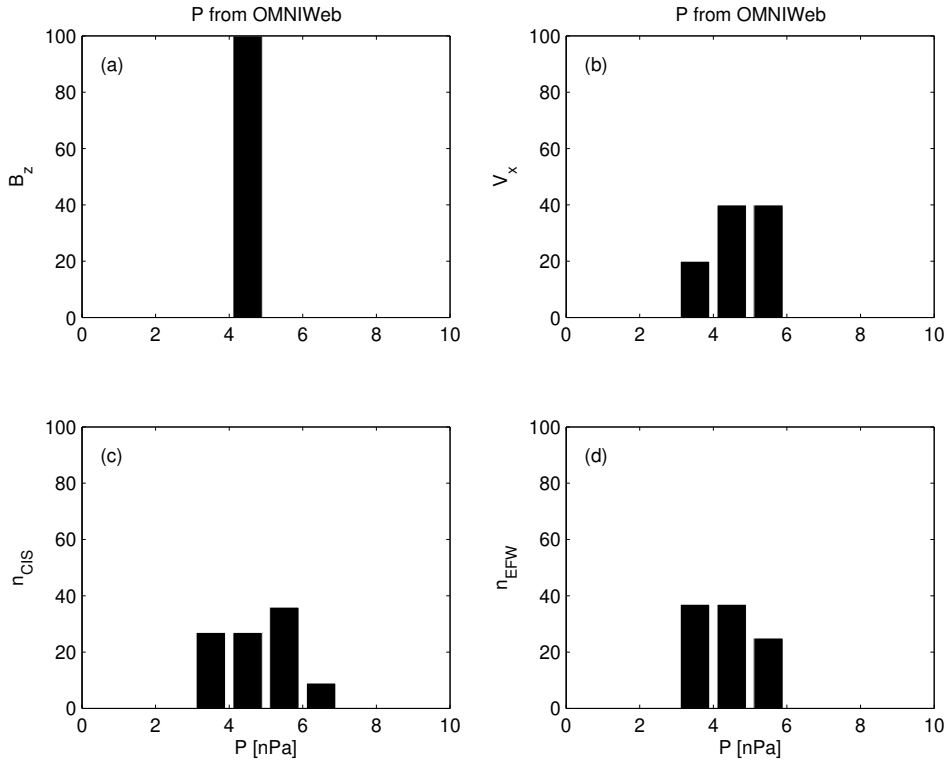
982      **Figure 13.** (a, b, c) The distributions of the OMNI solar wind magnetic field ( $B_x$ ,  $B_y$ ,  $B_z$ )  
 983      components, (d, e, f) the OMNI solar wind velocity ( $V_x$ ,  $V_y$ ,  $V_z$ ) components and (g) the solar  
 984      wind dynamic pressure during the 1-year run from January 29, 2002 to February 2, 2003 in GSE  
 985      reference frame, respectively. The relative values are given on the vertical axis of all plots in  
 986      percentage.



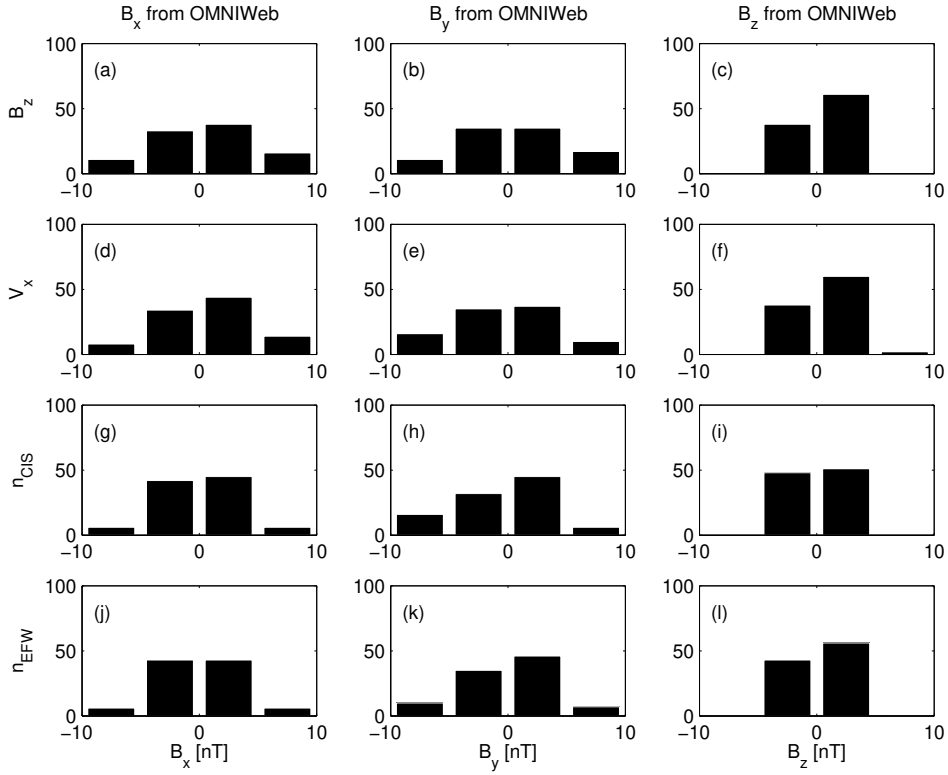
987 **Figure 14.** The distributions of the  $B_x$ , the  $B_y$  and the  $B_z$  OMNI solar wind magnetic field  
 988 components when the agreement of the Cluster SC3 measurements and the GUMICS-4 simu-  
 989 lations are poor in the solar wind (see Table 4). The  $B_z$ , the  $V_x$ , the  $n_{CIS}$  and the  $n_{EFW}$  are  
 990 the magnetic field GSE Z component, the plasma ion velocity X GSE component, the solar wind  
 991 density measured by the CIS HIA instrument and the calculated from the EFW spacecraft po-  
 992 tential, respectively. (a, b, c) Distribution of OMNI  $B_x$ ,  $B_y$ ,  $B_z$  when the agreement of  $B_z$  is  
 993 poor. (d, e, f) Distribution of OMNI  $B_x$ ,  $B_y$ ,  $B_z$  when the agreement of  $V_x$  is poor. (g, h, i)  
 994 Distribution of OMNI  $B_x$ ,  $B_y$ ,  $B_z$  when the agreement of  $n_{CIS}$  is poor. (j, k, l) Distribution of  
 995 OMNI  $B_x$ ,  $B_y$ ,  $B_z$  when the agreement of  $n_{EFW}$  is poor. The values are in percentage unit in  
 996 the distributions.



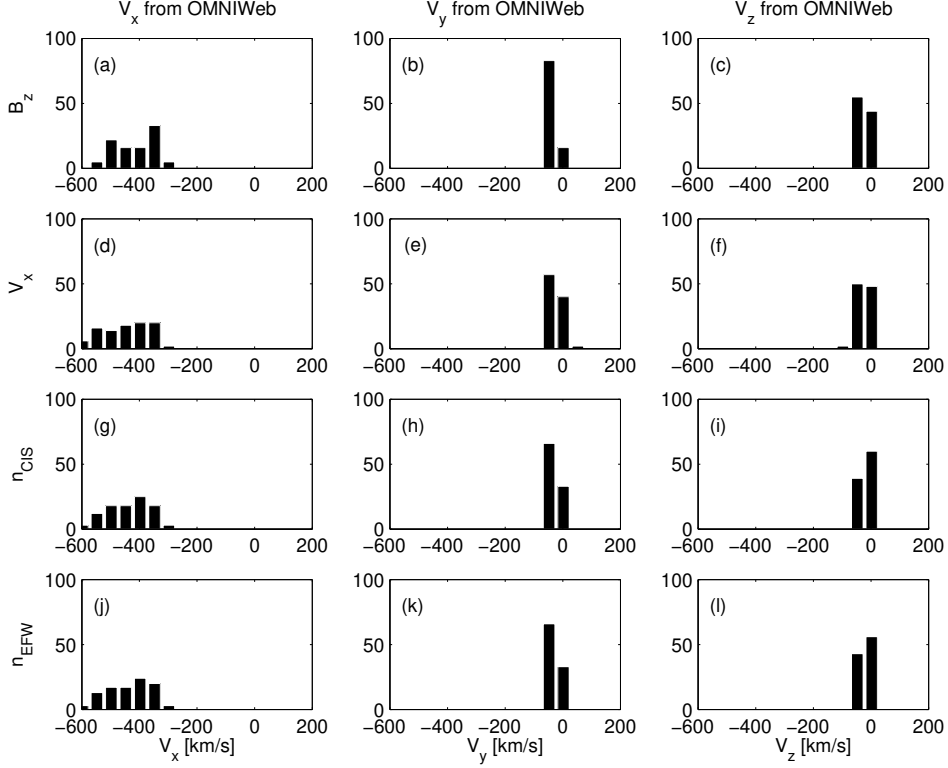
997 **Figure 15.** The distributions of the  $V_x$ , the  $V_y$  and the  $V_z$  OMNI solar wind magnetic field  
998 components when the agreement of the Cluster SC3 measurements and the GUMICS–4 simu-  
999 lations are poor in the solar wind (see Table 4). The  $B_z$ , the  $V_x$ , the  $n_{CIS}$  and the  $n_{EFW}$  are  
1000 the magnetic field GSE Z component, the plasma ion velocity X GSE component, the solar wind  
1001 density measured by the CIS HIA instrument and the calculated from the EFW spacecraft po-  
1002 tential, respectively. (a, b, c) Distribution of OMNI  $V_x$ ,  $V_y$ ,  $V_z$  when the agreement of  $B_z$  is poor.  
1003 (d, e, f) Distribution of OMNI  $V_x$ ,  $V_y$ ,  $V_z$  when the agreement of  $V_x$  is poor. (g, h, i) Distribution  
1004 of OMNI  $V_x$ ,  $V_y$ ,  $V_z$  when the agreement of  $n_{CIS}$  is poor. (j, k, l) Distribution of OMNI  $V_x$ ,  $V_y$ ,  
1005  $V_z$  when the agreement of  $n_{EFW}$  is poor. The values are in percentage unit in the distributions.



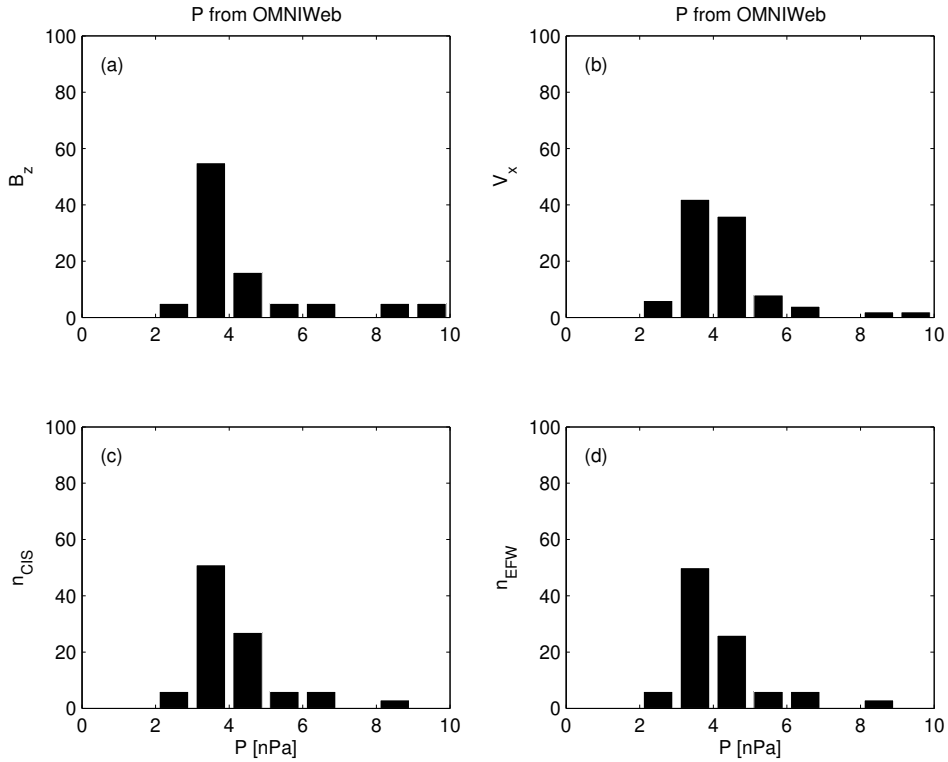
1006      **Figure 16.** The distributions of the  $P$  solar wind dynamic pressure calculated from OMNI  
 1007 parameters when the agreement of the Cluster SC3 measurements and the GUMICS–4 simula-  
 1008 tions are poor in the solar wind (see Table 4). The  $B_z$ ,  $V_x$ ,  $n_{CIS}$  and  $n_{EFW}$  are the magnetic  
 1009 field GSE Z component, the velocity X GSE component, the solar wind density measured by the  
 1010 CIS HIA instrument and calculated from the EFW spacecraft potential, respectively. (a, b, c, d)  
 1011 The distribution of the  $P$  calculated from OMNI data when the agreement of the  $B_z$ , the  $V_x$ , the  
 1012  $n_{CIS}$  or the  $n_{EFW}$  are poor. The values are in percentage unit in the distributions.



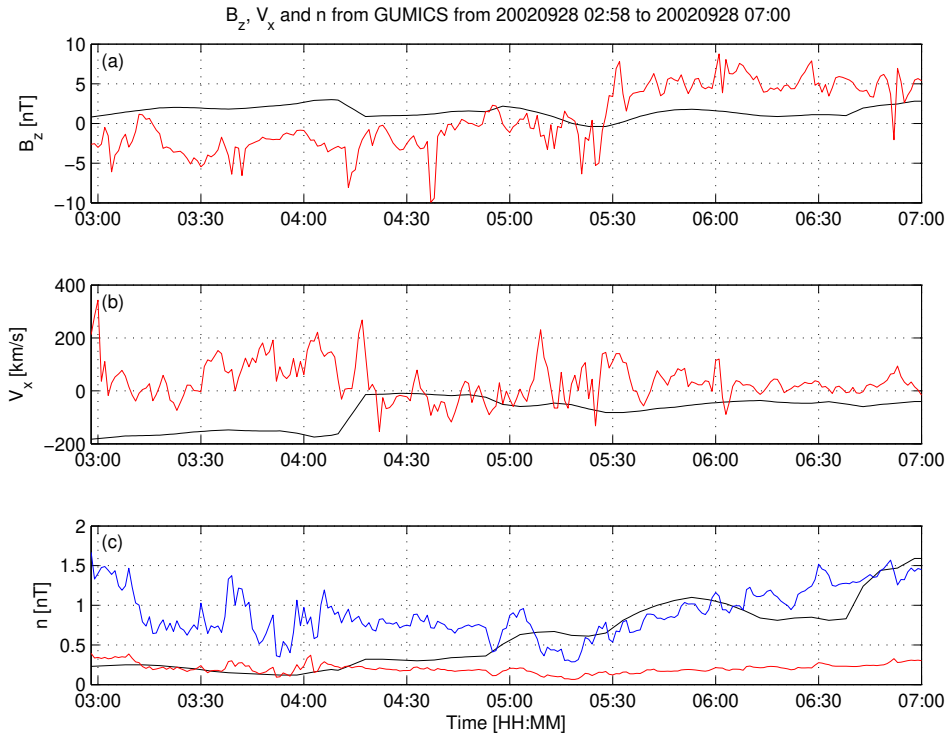
1013      **Figure 17.** The distributions of the  $B_x$ , the  $B_y$  and the  $B_z$  OMNI solar wind magnetic field  
 1014      components when the agreement of the Cluster SC3 measurements and the GUMICS–4 simu-  
 1015      lations are poor in the magnetosheath (see Table 5). The  $B_z$ , the  $V_x$ , the  $n_{CIS}$  and the  $n_{EFW}$   
 1016      are the magnetic field GSE Z component, the plasma ion velocity X GSE component, the solar  
 1017      wind density measured by the CIS HIA instrument and the calculated from the EFW spacecraf-  
 1018      t potential, respectively. (a, b, c) Distribution of OMNI  $B_x$ ,  $B_y$ ,  $B_z$  when the agreement of  $B_z$   
 1019      is poor. (d, e, f) Distribution of OMNI  $B_x$ ,  $B_y$ ,  $B_z$  when the agreement of  $V_x$  is poor. (g, h, i)  
 1020      Distribution of OMNI  $B_x$ ,  $B_y$ ,  $B_z$  when the agreement of  $n_{CIS}$  is poor. (j, k, l) Distribution of  
 1021      OMNI  $B_x$ ,  $B_y$ ,  $B_z$  when the agreement of  $n_{EFW}$  is poor. The values are in percentage unit in  
 1022      the distributions.



1023 **Figure 18.** The distributions of the  $V_x$ , the  $V_y$  and the  $V_z$  OMNI solar wind magnetic field  
 1024 components when the agreement of the Cluster SC3 measurements and the GUMICS–4 simula-  
 1025 tions are poor in the magnetosheath (see Table 5). The  $B_z$ , the  $V_x$ , the  $n_{CIS}$  and the  $n_{EFW}$  are  
 1026 the magnetic field GSE Z component, the plasma ion velocity X GSE component, the solar wind  
 1027 density measured by the CIS HIA instrument and the calculated from the EFW spacecraft po-  
 1028 tential, respectively. (a, b, c) Distribution of OMNI  $V_x$ ,  $V_y$ ,  $V_z$  when the agreement of  $B_z$  is poor.  
 1029 (d, e, f) Distribution of OMNI  $V_x$ ,  $V_y$ ,  $V_z$  when the agreement of  $V_x$  is poor. (g, h, i) Distribution  
 1030 of OMNI  $V_x$ ,  $V_y$ ,  $V_z$  when the agreement of  $n_{CIS}$  is poor. (j, k, l) Distribution of OMNI  $V_x$ ,  $V_y$ ,  
 1031  $V_z$  when the agreement of  $n_{EFW}$  is poor. The values are in percentage unit in the distributions.



1032 **Figure 19.** The distributions of the  $P$  solar wind dynamic pressure calculated from OMNI pa-  
 1033 rameters when the agreement of the Cluster SC3 measurements and the GUMICS-4 simulations  
 1034 are poor in the magnetosheath (see Table 5). The  $B_z$ ,  $V_x$ ,  $n_{CIS}$  and  $n_{EFW}$  are the magnetic  
 1035 field GSE Z component, the velocity X GSE component, the solar wind density measured by the  
 1036 CIS HIA instrument and calculated from the EFW spacecraft potential, respectively. (a, b, c, d)  
 1037 The distribution of the  $P$  calculated from OMNI data when the agreement of the  $B_z$ , the  $V_x$ , the  
 1038  $n_{CIS}$  or the  $n_{EFW}$  are poor. The values are in percentage unit in the distributions.



1039 **Figure 20.** GUMICS-4 simulation results (black) and Cluster SC3 magnetic field Z compo-  
 1040 nent, ion plasma moments (red) and electron density calculated from spacecraft potential (blue)  
 1041 from September 28, 2002 from 2:58 to 7:00 (UT) in the tail in GSE system. (a) Magnetic field  
 1042 Z component. (b) Solar wind velocity X component (c) Solar wind density. From 05:15 to 05:30  
 1043 both the Cluster SC3 and the virtual spaceprobe of the GUMICS-4 simulation cross the neutral  
 1044 sheet multiple times.

Start/End	$C_{B_z}$	$\delta t_{B_z}$	$C_{V_x}$	$\delta t_{V_x}$	$C_{n_{CIS}}$	$\delta t_{n_{CIS}}$	$C_{n_{EFW}}$	$\delta t_{n_{EFW}}$
	[min]		[min]		[min]		[min]	
20020201 20:00/0203 04:00	0.96	2	1.00	13	0.96	3	0.98	3
20020211 13:00/0212 12:00	0.82	2	1.00	0	0.99	18	0.99	18
20020218 09:00/0219 02:00	0.93	0	1.00	-3	0.94	-3	0.97	-3
20020219 06:30/0219 15:00	0.93	1	1.00	0	0.99	-60	1.00	-52
20020220 18:30/0222 00:00	0.87	4	1.00	4	0.93	-21	0.98	3
20020318 17:30/0319 02:30	0.89	1	1.00	21	0.98	50	0.99	5
20020412 20:30/0413 02:00	0.90	4	0.99	-54	0.94	60	0.98	12
20021227 12:00/1228 03:00	0.75	4	1.00	-3	0.99	-26	0.99	21
20021229 20:00/1230 16:00	0.68	1	1.00	1	0.99	-30	0.98	41
20030106 06:00/0106 19:00	0.79	4	1.00	6	0.99	4	0.99	-60
20030108 07:00/0109 03:30	0.55	10	1.00	41	0.99	10	0.97	-55
20030113 08:30/0113 18:00	0.91	3	1.00	5	1.00	3	0.97	-1
20030120 07:30/0120 13:00	0.82	2	1.00	9	1.00	-6	1.00	-3
20030122 12:00/0123 14:00	0.81	2	1.00	3	0.99	3	0.92	-60
20030124 18:00/0126 00:00	0.73	3	1.00	0	0.99	-60	0.99	60
20030127 16:00/0128 06:00	0.88	-1	1.00	-3	0.95	1	0.88	11
20030129 12:00/0130 18:00	0.90	2	1.00	4	0.94	-59	0.98	1

1045 **Table 1.** The studied solar wind intervals. The correlation coefficients ( $C_{B_z}$ ,  $C_{V_x}$ ,  $C_{n_{CIS}}$ ,  
1046  $C_{n_{EFW}}$ ) and time shift ( $\delta t_{V_x}$ ,  $\delta t_{n_{CIS}}$ ,  $\delta t_{n_{EFW}}$ ) in minutes of the magnetic field GSE Z compo-  
1047 nent ( $B_z$ ), solar wind velocity X component ( $V_x$ ), CIS and EFW densities ( $n_{CIS}$ ,  $n_{EFW}$ ).

Table 2: The studied magnetosheath intervals. The correlation coefficients ( $C_{B_z}$ ,  $C_{V_x}$ ,  $C_{n_{CIS}}$ ,  $C_{n_{EFW}}$ ) and time shift ( $\delta t_{V_x}$ ,  $\delta t_{n_{CIS}}$ ,  $\delta t_{n_{EFW}}$ ) in minutes of the magnetic field GSE Z component ( $B_z$ ), solar wind velocity X component ( $V_x$ ), CIS and EFW densities ( $n_{CIS}$ ,  $n_{EFW}$ ). In the empty slots the correlation calculation gives invalid result.

Start/End	$C_{B_z}$	$\delta t_{B_z}$	$C_{V_x}$	$\delta t_{V_x}$	$C_{n_{CIS}}$	$\delta t_{n_{CIS}}$	$C_{n_{EFW}}$	$\delta t_{n_{EFW}}$
		[min]		[min]		[min]		[min]
20020201 13:30/0201 18:30	0.91	1	0.98	56	0.99	60	0.976	60
20020208 18:15/0209 00:00	0.73	2	0.95	60	0.98	-52	0.98	-54
20020211 02:30/0211 09:00	0.79	0	0.99	-20	0.99	-1	0.99	1
20020212 16:30/0212 21:00	0.80	3	0.99	54	0.99	31	0.99	30
20020219 17:30/0219 23:00	0.76	4	0.98	37	0.99	7	0.99	6
20020222 23:00/0223 06:30	0.64	0	0.97	-60	0.99	-47	0.98	-48
20020227 16:30/0227 23:15	0.48	59	0.98	-31	0.99	-39	1.00	-12
20020310 18:30/0311 00:30	0.97	3	0.98	19	0.99	8	0.99	-2
20020311 14:00/0311 19:00	0.86	5	0.97	36	0.99	-3	0.99	-40
20020406 19:00/0407 01:15	0.76	2	0.96	-60	0.98	-55	0.98	-56
20020410 17:30/0410 23:00	0.89	6	0.99	-50	0.99	3	1.00	5
20020411 11:30/0411 16:30	0.82	4	0.99	39	0.99	3	0.99	3
20020418 18:30/0418 22:45	0.92	60	0.99	-60	0.99	60	0.98	60
20020421 04:30/0421 07:45	0.96	47	0.99	-60	1.00	-60	1.00	-60
20020422 11:45/0422 15:45	0.73	-5	0.98	-17	0.99	-15	0.98	-16
20020423 08:30/0423 12:30	0.93	31	0.99	3	0.99	16	0.99	16
20020430 12:30/0430 17:00	0.79	59	0.98	22	0.98	-18		
20020505 07:00/0505 11:15	0.71	59	0.99	-58	0.98	-60		
20020506 19:15/0507 00:15	0.84	-27	0.98	-60	0.97	-37		
20020507 17:30/0507 23:00	0.93	2	0.98	-30	0.99	-49		
20020514 22:45/0515 03:00	0.79	49	0.99	35	0.99	38	0.99	43
20020517 07:00/0517 12:15	0.74	-5	1.00	-5	0.99	-4	0.99	-3
20020518 13:30/0518 19:30	0.70	1	0.99	9	0.97	-1	0.97	-1

*Continued on next page*

Table 2 – *Continued from previous page*

Start/End	$C_{B_z}$	$\delta t_{B_z}$	$C_{V_x}$	$\delta t_{V_x}$	$C_{n_{CIS}}$	$\delta t_{n_{CIS}}$	$C_{n_{EFW}}$	$\delta t_{n_{EFW}}$
		[min]		[min]		[min]		[min]
20020519 20:00/0520 03:30	0.98	2	1.00	-9	0.99	-5	0.99	-50
20020520 10:45/0520 20:15	0.77	1	0.99	-3	0.95	-1	0.99	-1
20020522 02:00/0522 08:45	0.49	52	0.99	4	0.99	12	0.99	22
20020527 02:15/0527 17:15	0.79	-3	0.99	-3	0.98	0	0.98	0
20020530 05:00/0530 10:30	0.29	3	1.00	-38	0.99	3	0.99	3
20020601 19:30/0602 01:00	0.68	-2	1.00	18	0.99	-6	0.99	-7
20020602 21:45/0603 17:45	0.62	-5	0.99	-1	0.98	2	0.99	2
20020605 10:30/0606 06:00	0.18	0	1.00	-7	0.97	10	0.98	9
20020607 18:00/0607 22:00	0.92	-35	1.00	-36	0.99	16	0.99	16
20020608 01:15/0608 18:15	0.53	-4	0.99	-39	0.96	-6	0.97	-6
20020610 01:30/0610 09:30	0.76	5	0.99	8	0.99	-5	0.99	-7
20020610 11:00/0611 01:00	0.87	-4	0.99	-33	0.98	23	0.99	6
20020612 18:30/0613 06:15	0.44	-2	0.99	-7	0.97	4	0.97	-32
20020615 07:00/0615 23:30			1.00	47	0.98	-3	0.98	-3
20020617 05:00/0618 03:45	0.76	4	1.00	28	0.98	10	0.98	8
20020620 04:00/0620 11:00	0.61	-8	0.99	-6	0.97	12	0.98	4
20020622 14:30/0622 18:00	0.98	55	1.00	35	0.99	16	1.00	16
20021201 04:15/1202 07:45	0.38	1	1.00	2	0.99	6	0.99	6
20021203 15:30/1204 19:30	0.67	1	0.99	60	0.98	59	0.98	59
20021207 00:30/1207 07:45	0.49	37	0.98	-56	0.99	-19	0.99	-4
20021208 09:30/1209 08:00	0.69	2	0.98	-35	0.97	6	0.98	4
20021212 23:30/1213 14:30	0.51	5	1.00	36	0.99	-3	0.81	-56
20021213 21:15/1214 09:30	0.93	5	0.99	-35	0.99	-13	0.99	-47
20021215 12:45/1216 18:00	0.76	2	0.99	-60	0.94	-60	0.98	31
20021217 16:30/1218 01:45	0.99	2	1.00	-54	0.99	3	0.99	3
20021220 01:30/1220 06:15	0.92	0	1.00	60	0.99	2	0.99	3
20021223 02:15/1223 13:00	0.91	1	0.97	49	0.93	49	0.99	-14
20021223 14:00/1223 22:30	0.84	1	0.99	-2	0.99	-1	1.00	-3
20021224 19:00/1225 01:45	0.94	0	1.00	-44	0.99	26	0.99	27

*Continued on next page*

Table 2 – *Continued from previous page*

Start/End	$C_{B_z}$	$\delta t_{B_z}$	$C_{V_x}$	$\delta t_{V_x}$	$C_{n_{CIS}}$	$\delta t_{n_{CIS}}$	$C_{n_{EFW}}$	$\delta t_{n_{EFW}}$
		[min]		[min]		[min]		[min]
20021225 23:45/1226 07:15	0.96	7	1.00	-17	0.99	56	0.99	55
20021226 23:00/1227 09:45	0.79	2	1.00	2	0.98	4	0.99	3
20021229 11:45/1229 17:00	0.60	2	1.00	-60	0.98	-19	0.98	50
20021230 17:45/1231 01:00	0.69	1	0.98	52	0.98	60	0.98	22
20021231 23:00/0101 05:15	0.89	2	0.99	15	0.99	-54	1.00	-58
20030105 14:00/0105 21:00	0.69	0	0.99	1	0.98	-60	0.99	-60
20030106 23:15/0107 03:00	0.52	9	0.98	60	0.99	56	1.00	-60
20030109 08:45/0109 16:15			0.91	-56	0.98	-13	0.98	-26
20030110 07:15/0110 15:15	0.94	1	0.99	-7	0.99	1	0.98	5
20030111 08:15/0111 22:30	0.84	0	0.99	-59	0.94	-15	0.94	8
20030112 17:30/0113 00:15	0.98	0	1.00	-52	0.99	39	0.99	51
20030114 00:30/0114 08:30	0.84	-1	0.99	-60	0.98	23	0.98	8
20030116 10:15/0116 17:45	0.62	60	0.93	52	0.99	60	0.99	30
20030117 09:30/0117 13:30	0.68	-3	1.00	8	1.00	-31	0.99	-33
20030118 23:30/0119 03:45	0.93	3	1.00	-12	1.00	7	0.99	7
20030119 21:00/0120 01:00	0.94	3	1.00	5	1.00	38	1.00	19
20030121 06:30/0121 11:30	0.82	-15	0.96	47	0.98	7	0.99	-39
20030122 04:45/0122 09:30	0.69	-2	1.00	10	0.99	-9	0.99	-5
20030126 01:45/0126 06:30	0.85	3	0.99	-15	0.99	-50	0.99	23
20030127 08:15/0127 13:00	1.00	9	1.00	-60	0.98	0	0.99	1
20030128 12:30/0128 17:15	0.77	60	0.99	-24	0.99	-6	0.988	20
20030130 19:45/0131 00:15	0.98	2	0.99	51	0.99	25	0.99	9

Table 3: The studied magnetosphere intervals (UT).

Start/End
20020213 23:00/0214 01:30
20020217 18:30/0218 02:00
20020220 00:45/0220 12:00
20020222 11:15/0222 20:15
20020225 02:15/0225 08:30
20020227 06:00/0227 12:00
20020302 00:00/0302 03:15
20020306 10:00/0306 18:30
20020308 17:30/0309 06:00
20020311 02:15/0311 12:00
20020313 11:15/0314 00:15
20020316 04:45/0316 08:00
20020318 09:00/0318 14:45
20020320 20:30/0320 23:55
20020323 04:00/0323 09:45
20020327 23:45/0328 06:15
20020330 07:15/0330 12:45
20020401 19:30/0401 22:00
20020406 09:30/0406 18:00
20020408 15:00/0409 00:00
20020410 23:30/0411 09:45
20020413 08:30/0413 19:00
20020416 18:00/0417 04:30
20020418 06:00/0418 12:00
20020420 15:00/0420 23:00
20020422 20:00/0423 07:00
20020425 08:30/0425 18:00
20020430 04:40/0430 12:00
20020504 14:30/0504 16:45

*Continued on next page*

Table 3 – *Continued from previous page*

Start/End
20020505 02:30/0505 07:00
20020507 01:30/0507 15:45
20020508 11:00/0510 04:15
20020512 02:45/0512 09:30
20020514 10:30/0514 12:45
20020519 00:30/0519 19:30
20020521 01:30/0521 22:00
20020523 23:30/0524 02:00
20020524 19:00/0525 08:15
20020526 07:30/0526 10:30
20020528 20:00/0529 05:00
20020531 02:15/0531 13:30
20020602 04:30/0602 07:30
20020602 12:00/0602 21:30
20020604 08:30/0605 07:00
20020606 14:30/0607 16:30
20020609 06:00/0609 20:00
20020611 11:00/0612 13:00
20020614 01:00/0614 16:00
20020616 08:00/0616 18:00
20020620 13:30/0622 01:00
20020623 13:00/0623 17:00
20020624 04:00/0624 10:15
20020630 17:45/0701 15:00
20020701 21:00/0703 10:30
20020703 23:00/0706 03:15
20020707 01:00/0708 23:00
20020710 11:30/0714 03:30
20020714 15:45/0715 15:30
20020716 23:30/0717 16:00

*Continued on next page*

Table 3 – *Continued from previous page*

Start/End
20020718 05:45/0722 11:00
20020722 23:45/0728 01:00
20020728 02:00/0804 03:45
20020804 04:45/0811 06:15
20020811 07:30/0816 01:00
20020816 15:30/0818 09:00
20020818 10:00/0825 11:30
20020825 13:00/0901 14:15
20020901 17:15/0903 23:30
20020905 02:15/0906 16:30
20020907 10:30/0908 17:00
20020908 18:00/0915 19:30
20020915 21:00/0922 22:30
20020923 00:00/0923 23:30
20020924 03:30/0928 22:45
20020928 23:30/0930 01:00
20020930 02:15/1006 17:00
20021006 17:45/1007 03:30
20021007 05:00/1007 17:30
20021008 07:30/1010 22:00
20021010 22:30/1012 22:30
20021012 23:00/1014 06:30
20021014 09:00/1016 04:00
20021016 14:00/1019 00:15
20021019 01:30/1019 22:00
20021021 04:00/1022 19:30
20021022 22:30/1026 02:30
20021026 04:00/1029 20:15
20021030 01:30/1102 08:00
20021102 22:00/1104 22:00

*Continued on next page*

Table 3 – *Continued from previous page*

Start/End
20021106 00:00/1107 18:00
20021108 02:00/1109 18:45
20021111 00:00/1112 01:30
20021113 03:45/1114 14:15
20021115 20:30/1116 23:00
20021118 01:00/1118 23:30
20021120 17:00/1121 06:00
20021122 21:30/1124 01:00
20021125 04:00/1126 08:30
20021127 20:00/1128 18:30
20021130 04:00/1201 01:30
20021202 14:30/1203 09:00
20021204 22:00/1205 19:30
20021207 09:00/1207 16:30
20021207 18:00/1207 22:00
20021209 16:30/1210 14:30
20021212 13:45/1212 21:30
20021214 13:30/1214 20:00
20021214 21:00/1215 07:30
20021216 21:00/1217 15:00
20021219 08:00/1219 19:30
20021221 15:45/1221 23:15
20021222 00:30/1222 08:45
20021224 02:30/1224 14:00
20021226 10:00/1226 19:00
20021228 19:30/1229 02:30
20021229 04:00/1229 10:00
20021231 05:00/1231 18:45
20030102 12:30/0102 20:45
20030104 20:45/0105 06:00

*Continued on next page*

Table 3 – *Continued from previous page*

Start/End
20030105 07:00/0105 13:30
20030107 05:45/0107 21:00
20030109 17:00/0110 00:45
20030112 00:00/0112 09:15
20030112 10:30/0112 16:00
20030114 11:00/0114 20:00
20030116 20:30/0116 22:45
20030119 04:30/0119 09:30
20030119 14:00/0119 17:00
20030121 13:30/0121 21:30
20030126 07:30/0126 15:45
20030128 17:45/0129 08:15
20030131 01:30/0131 11:45

Start/End	OMNI			Cluster SC3			
	$B_z$ [nT]	$V_x$ [km/s]	P [cm $^{-3}$ ]	$B_z$	$V_x$	$n_{CIS}$	$n_{EFW}$
20020201 20:00/0203 04:00	-1.25	-373.52	4.08	y	y	n	y
20020211 13:00/0212 12:00	0.03	-533.11	2.18	y	y	y	y
20020218 09:00/0219 02:00	2.56	-362.41	3.46	y	n	n	y
20020219 06:30/0219 15:00	3.55	-401.63	1.25	y	y	n	n
20020220 18:30/0222 00:00	1.95	-440.18	1.96	y	y	n	y
20020318 17:30/0319 02:30	3.79	-429.30	15.34	y	n	n	n
20020412 20:30/0413 02:00	-1.81	-420.35	3.24	y	n	n	y
20021227 12:00/1228 03:00	0.09	-714.40	2.72	y	n	n	y
20021229 20:00/1230 16:00	-0.37	-526.40	2.26	y	y	n	n
20030106 06:00/0106 19:00	2.25	-399.91	1.50	y	n	n	n
20030108 07:00/0109 03:30	-0.58	-280.80	2.97	n	n	y	n
20030113 08:30/0113 18:00	0.68	-397.83	1.72	y	y	y	n
20030120 07:30/0120 13:00	2.16	-630.69	2.43	y	y	y	y
20030122 12:00/0123 14:00	0.13	-608.96	3.41	y	y	y	n
20030124 18:00/0126 00:00	-0.71	-739.68	2.87	y	y	n	n
20030127 16:00/0128 06:00	-0.92	-451.84	3.12	y	y	n	n
20030129 12:00/0130 18:00	-3.09	-450.00	3.96	y	y	n	y

1050      **Table 4.** The average OMNI input parameters in the solar wind and the good/bad agreement  
 1051      of the GUMICS–4 simulations to the Cluster  $B_z$  magnetic field component, the  $V_x$  solar wind  
 1052      speed component, the  $n_{CIS}$  solar wind density measured by the Cluster CIS HIA instrument and  
 1053      the  $n_{EFW}$  solar wind density calculated from the spacecraft potential measured by the Cluster  
 1054      EFW instrument in the solar wind.

Table 5: The average OMNI input parameters in the solar wind and the good/bad agreement of the GUMICS–4 simulations to the Cluster  $B_z$  magnetic field component, the  $V_x$  solar wind speed component, the  $n_{CIS}$  solar wind density measured by the Cluster CIS HIA instrument and the  $n_{EFW}$  solar wind density calculated from the spacecraft potential measured by the Cluster EFW instrument in the magnetosheath.

Start/End	OMNI			Cluster SC3			
	$B_z$	$V_x$	P	$B_z$	$V_x$	$n_{CIS}$	$n_{EFW}$
	[nT]	[km/s]	[cm $^{-3}$ ]				
20020201 13:30/0201 18:30	0.19	-342.87	4.62	y	n	n	n
20020208 18:15/0209 00:00	-0.48	-508.16	1.61	y	n	n	n
20020211 02:30/0211 09:00	-1.85	-425.67	1.78	y	y	y	y
20020212 16:30/0212 21:00	2.98	-509.22	2.34	y	n	n	n
20020219 17:30/0219 23:00	1.46	-431.50	1.46	y	y	y	y
20020222 23:00/0223 06:30	0.86	-391.22	1.14	y	n	n	n
20020227 16:30/0227 23:15	1.89	-343.13	1.52	n	n	n	n
20020310 18:30/0311 00:30	-2.81	-379.46	1.78	y	y	y	y
20020311 14:00/0311 19:00	1.63	-371.43	2.68	n	n	n	n
20020406 19:00/0407 01:15	-2.71	-333.13	0.93	y	n	n	n
20020410 17:30/0410 23:00	0.31	-312.43	4.42	n	n	y	y
20020411 11:30/0411 16:30	-1.50	-494.02	4.25	y	y	n	n
20020418 18:30/0418 22:45	-0.92	-450.82	0.30	n	n	n	n
20020421 04:30/0421 07:45	0.40	-455.69	1.37	n	n	n	n
20020422 11:45/0422 15:45	0.25	-419.98	1.14	n	n	y	y
20020423 08:30/0423 12:30	2.77	-507.99	6.82	n	n	n	n
20020430 12:30/0430 17:00	2.15	-479.51	3.02	n	n	n	n
20020505 07:00/0505 11:15	0.20	-336.81	1.74	n	n	n	n
20020506 19:15/0507 00:15	0.78	-390.00	2.46	y	n	n	n
20020507 17:30/0507 23:00	2.87	-392.40	3.49	y	n	n	n
20020514 22:45/0515 03:00	-2.42	-414.01	1.82	n	n	n	n

*Continued on next page*

Table 5 – *Continued from previous page*

Start/End	OMNI			Cluster SC3			
	$B_z$ [nT]	$V_x$ [km/s]	P $[cm^{-3}]$	$B_z$	$V_x$	$n_{CIS}$	$n_{EFW}$
20020517 07:00/0517 12:15	-0.39	-379.32	1.52	y	y	y	y
20020518 13:30/0518 19:30	0.63	-345.87	1.59	n	n	y	y
20020519 20:00/0520 03:30	4.75	-408.56	1.12	y	y	y	y
20020520 10:45/0520 20:15	0.74	-448.89	1.93	y	y	y	y
20020522 02:00/0522 08:45	-1.07	-398.12	1.63	n	y	y	y
20020527 02:15/0527 17:15	-3.11	-542.53	2.07	y	y	y	y
20020530 05:00/0530 10:30	0.03	-493.86	2.08	y	n	y	y
20020601 19:30/0602 01:00	-3.38	-342.27	4.16	y	y	y	y
20020602 21:45/0603 17:45	0.38	-435.47	1.89	y	y	y	y
20020605 10:30/0606 06:00	-0.42	-394.49	1.08	y	y	n	n
20020607 18:00/0607 22:00	-1.60	-291.85	1.80	y	y	y	y
20020608 01:15/0608 18:15	0.06	-335.39	2.74	y	n	y	y
20020610 01:30/0610 09:30	1.60	-465.52	3.00	y	y	y	y
20020610 11:00/0611 01:00	-2.27	-419.86	2.16	y	n	y	y
20020612 18:30/0613 06:15	-1.13	-351.03	1.16	y	y	y	y
20020615 07:00/0615 23:30	-1.16	-334.27	2.84	n	n	y	y
20020617 05:00/0618 03:45	0.78	-351.47	1.87	y	n	y	y
20020620 04:00/0620 11:00	0.46	-485.48	1.73	y	y	y	y
20020622 14:30/0622 18:00	-0.72	-429.02	1.93	n	n	y	y
20021201 04:15/1202 07:45	-1.09	-499.23	2.62	y	y	y	y
20021203 15:30/1204 19:30	0.34	-449.09	2.06	y	n	n	n
20021207 00:30/1207 07:45	0.80	-451.80	7.33	n	n	y	y
20021208 09:30/1209 08:00	0.60	-600.27	1.49	y	n	y	y
20021212 23:30/1213 14:30	0.10	-337.77	1.32	y	n	n	n
20021213 21:15/1214 09:30	-0.74	-361.19	2.99	y	n	y	y
20021215 12:45/1216 18:00	1.32	-479.48	1.53	y	n	n	n
20021217 16:30/1218 01:45	4.56	-393.99	2.49	y	n	y	y
20021220 01:30/1220 06:15	-1.21	-530.62	3.01	y	n	y	y

*Continued on next page*

Table 5 – *Continued from previous page*

Start/End	OMNI			Cluster SC3			
	$B_z$ [nT]	$V_x$ [km/s]	P $[cm^{-3}]$	$B_z$	$V_x$	$n_{CIS}$	$n_{EFW}$
20021223 02:15/1223 13:00	-2.32	-516.12	2.22	y	n	n	n
20021223 14:00/1223 22:30	0.89	-519.77	2.55	y	y	y	y
20021224 19:00/1225 01:45	0.88	-523.86	3.41	y	n	y	y
20021225 23:45/1226 07:15	-0.61	-414.38	2.21	y	y	n	n
20021226 23:00/1227 09:45	-1.79	-618.14	6.20	y	y	y	y
20021229 11:45/1229 17:00	-0.41	-580.12	2.39	y	n	n	n
20021230 17:45/1231 01:00	-1.01	-483.60	1.93	y	n	n	y
20021231 23:00/0101 05:15	0.60	-418.95	1.94	y	n	n	n
20030105 14:00/0105 21:00	-0.03	-414.46	1.69	y	n	n	n
20030106 23:15/0107 03:00	-1.62	-392.29	1.56	n	n	n	n
20030109 08:45/0109 16:15	1.45	-272.82	2.31	n	n	n	n
20030110 07:15/0110 15:15	-2.11	-401.03	2.72	y	n	y	y
20030111 08:15/0111 22:30	-0.20	-433.33	1.24	y	n	n	y
20030112 17:30/0113 00:15	1.53	-389.62	1.45	y	n	n	n
20030114 00:30/0114 08:30	-1.67	-388.53	2.27	y	n	n	y
20030116 10:15/0116 17:45	-1.20	-328.91	1.22	n	n	n	n
20030117 09:30/0117 13:30	-1.36	-327.09	2.55	y	y	y	y
20030118 23:30/0119 03:45	6.41	-459.46	4.82	y	y	y	y
20030119 21:00/0120 01:00	1.52	-597.95	2.38	y	n	y	y
20030121 06:30/0121 11:30	-1.77	-670.25	1.50	y	n	n	n
20030122 04:45/0122 09:30	0.11	-588.87	2.30	y	n	y	y
20030126 01:45/0126 06:30	-0.24	-713.82	2.75	y	y	y	y
20030127 08:15/0127 13:00	7.94	-509.30	0.47	y	n	y	y
20030128 12:30/0128 17:15	4.95	-443.83	4.15	y	y	y	y
20030130 19:45/0131 00:15	4.21	-510.33	2.63	y	n	y	y

Table 6: Intervals around the studied bow shock crossings. The Cluster SC3 crossed the bow shock in all cases. The 2nd column shows whether the bow shock is visible in the GUMICS–4 simulations.

Start/End	GUMICS Bow Shock
20020201 12:00/0202 00:00	+
20020203 00:00/0203 12:00	+
20020206 06:00/0206 18:00	+
20020208 18:00/0209 06:00	+
20020211 06:00/0211 18:00	+
20020212 12:00/0212 18:00	+
20020213 12:00/0213 18:00	+
20020216 00:00/0216 12:00	+
20020217 06:00/0217 12:00	-
20020218 06:00/0218 18:00	+
20020219 00:00/0219 18:00	+
20020220 12:00/0221 00:00	+
20020221 18:00/0222 00:00	+
20020301 06:00/0301 12:00	+
20020304 12:00/0304 18:00	+
20020306 00:00/0306 06:00	+
20020307 00:00/0307 06:00	+
20020308 06:00/0308 12:00	+
20020309 06:00/0309 12:00	+
20020310 12:00/0311 00:00	+
20020311 18:00/0312 00:00	+
20020313 00:00/0313 06:00	-
20020314 00:00/0314 12:00	+
20020316 06:00/0316 18:00	+
20020318 12:00/0319 00:00	+
20020323 12:00/0323 18:00	+

*Continued on next page*

Table 6 – *Continued from previous page*

Start/End	GUMICS Bow Shock
20020325 18:00/0326 06:00	–
20020327 06:00/0327 12:00	+
20020329 18:00/0330 00:00	–
20020402 00:00/0402 06:00	+
20020405 18:00/0406 00:00	–
20020407 00:00/0407 06:00	–
20020409 06:00/0409 12:00	–
20020410 12:00/0410 18:00	–
20020411 12:00/0411 18:00	–
20020413 00:00/0413 06:00	+
20020413 18:00/0414 06:00	+
20020420 00:00/0420 06:00	+
20020423 12:00/0423 23:00	+
20020427 00:00/0427 06:00	+
20020428 06:00/0428 12:00	+
20020430 18:00/0501 00:00	+
20020505 06:00/0505 18:00	–
20020507 18:00/0509 06:00	+
20020510 06:00/0510 12:00	+
20020513 12:00/0513 18:00	+
20020515 00:00/0515 06:00	–
20020520 00:00/0520 06:00	+
20020522 06:00/0522 12:00	+
20020522 18:00/0523 06:00	+
20021206 06:00/1207 06:00	+
20021218 00:00/1219 00:00	+
20021220 18:00/1221 00:00	+
20021221 00:00/1221 12:00	+
20021222 12:00/1223 00:00	+
20021223 00:00/1223 06:00	+

*Continued on next page*

Table 6 – *Continued from previous page*

Start/End	GUMICS Bow Shock
20021225 06:00/1226 00:00	+
20021227 06:00/1228 00:00	+
20021228 00:00/1228 12:00	+
20021229 12:00/1230 00:00	+
20030101 06:00/0102 00:00	+
20030103 06:00/0103 12:00	+
20030104 00:00/0104 18:00	+
20030106 00:00/0107 00:00	+
20030108 00:00/0108 12:00	+
20030113 00:00/0114 06:00	+
20030115 00:00/0115 12:00	+
20030118 18:00/0119 00:00	+
20030120 00:00/0121 12:00	+
20030122 06:00/0122 12:00	+
20030123 12:00/0124 00:00	+
20030124 12:00/0124 18:00	+
20030126 00:00/0126 06:00	+
20030127 00:00/0127 18:00	+
20030128 06:00/0128 18:00	+
20030129 06:00/0129 12:00	+
20030130 18:00/0131 00:00	+

Table 7: Intervals around the studied magnetopause crossings.  
The Cluster SC3 crossed the magnetopause in all cases. The  
2nd column shows whether the magnetopause is visible in the  
GUMICS–4 simulations.

Start/End	GUMICS Magnetopause
20020203 06:00/0203 12:00	+
20020206 06:00/0206 12:00	-
20020211 00:00/0211 06:00	+
20020218 00:00/0218 06:00	+
20020225 06:00/0225 12:00	+
20020302 00:00/0302 06:00	+
20020306 18:00/0307 00:00	-
20020308 12:00/0308 18:00	-
20020311 12:00/0311 18:00	+
20020313 18:00/0314 00:00	-
20020314 00:00/0314 06:00	+
20020323 06:00/0323 12:00	+
20020330 12:00/0330 18:00	-
20020404 06:00/0404 12:00	-
20020409 00:00/0409 06:00	-
20020418 12:00/0418 18:00	+
20020422 12:00/0422 18:00	-
20020429 18:00/0430 00:00	-
20020507 12:00/0507 18:00	-
20020509 06:00/0509 12:00	-
20020510 00:00/0510 06:00	-
20020514 18:00/0515 00:00	-
20020519 12:00/0519 18:00	-
20020520 12:00/0521 00:00	-
20020522 00:00/0522 06:00	-
20020529 00:00/0529 12:00	-

*Continued on next page*

Table 7 – *Continued from previous page*

Start/End	GUMICS Magnetopause
20020530 06:00/0530 18:00	–
20020531 18:00/0601 00:00	–
20020602 18:00/0603 00:00	–
20020604 06:00/0604 12:00	–
20020605 06:00/0606 18:00	–
20020607 12:00/0608 06:00	+
20020609 00:00/0609 06:00	–
20020610 00:00/0610 06:00	–
20020611 00:00/0611 12:00	–
20020612 06:00/0614 00:00	–
20020614 18:00/0615 06:00	–
20020616 00:00/0616 12:00	+
20020620 00:00/0620 18:00	–
20020622 06:00/0622 18:00	–
20020704 12:00/0705 00:00	–
20020706 00:00/0706 12:00	+
20020709 00:00/0709 18:00	–
20020715 18:00/0716 12:00	–
20030105 06:00/0105 18:00	+
20030110 00:00/0110 12:00	+
20030112 12:00/0112 18:00	–
20030117 06:00/0117 12:00	+
20030121 06:00/0121 12:00	+
20030122 00:00/0122 06:00	–
20030126 18:00/0127 00:00	+
20030128 12:00/0128 18:00	+
20030129 00:00/0129 12:00	+
20030131 12:00/0201 00:00	+

Start/End	GUMICS Neutral Sheet
20020901 19:10/0901 23:54	–
20020906 14:07/0906 16:37	+
20020913 17:33/0913 20:06	+
20020918 12:47/0918 14:26	–
20020920 20:36/0921 02:13	+
20020928 02:58/0928 07:00	+
20021002 16:12/1002 23:52	–
20021014 12:34/1014 22:53	+
20021017 03:08/1017 04:11	–

1058      **Table 8.** Intervals around the studied neutral sheet crossings in the tail. The Cluster SC3  
 1059      crossed the neutral sheet in all cases. The 2nd column shows whether the neutral sheet is visible  
 1060      in the GUMICS–4 simulations.